In vitro coinfection by influenza A virus and respiratory syncytial virus generates hybrid viral particles with altered structure and tropism

Authors: Joanne Haney[1], Swetha Vijayakrishnan[1], James Streetley[2], Kieran Dee[1], Daniel Max Goldfarb[1], Mairi Clarke[2], Margaret Mullin[3], Stephen D Carter[1], David Bhella[1,2] and Pablo R Murcia[1]

Affiliations:

[1]MRC-University of Glasgow Centre for Virus Research, Institute of Infection, Immunity and Inflammation, College of Medical, Veterinary and Life Sciences, University of Glasgow, Glasgow, Scotland, UK.

[2]Scottish Centre for Macromolecular Imaging, College of Medical, Veterinary and Life Sciences, University of Glasgow, Glasgow, Scotland, UK.

[3]Glasgow Imaging Facility, Institute of Infection, Immunity and Inflammation, College of Medical, Veterinary and Life Sciences, University of Glasgow, Glasgow, Scotland, UK.

Correspondence: Pablo.Murcia@Glasgow.ac.uk

Abstract

Interactions between respiratory viruses impact viral transmission dynamics and clinical outcomes. To identify and characterize virus-virus interactions at the cellular level, we coinfected human lung cells with influenza A virus (IAV) and respiratory syncytial virus (RSV). Super-resolution microscopy, live-cell imaging, scanning electron microscopy, and cryo-electron tomography revealed extracellular and membrane-associated filamentous structures consistent with hybrid viral particles (HVPs). We show that HVPs harbor surface glycoproteins and ribonucleoproteins of IAV and RSV, and use the RSV fusion glycoprotein to evade anti-IAV neutralising antibodies and to infect and spread among cells lacking IAV receptors. Finally, we show evidence of IAV and RSV coinfection within cells of the bronchial epithelium, with viral proteins from both viruses co-localising at the apical surface. Our observations have profound implications for infection biology as they define a previously unknown interaction between respiratory viruses that might affect virus pathogenesis by expanding virus tropism and facilitating immune evasion.

Main Text

Viruses are intracellular pathogens whose replication relies on the infection of a restricted subset of cell types, a property known as tropism. As multiple viruses exhibit the same tropism, cells and tissues are susceptible to infection by a community of taxonomically diverse viruses. From this perspective, a tissue or body compartment constitutes an ecological niche in which members of a virus community co-exist. Coinfections by more than one virus represent between ~10-30% of all respiratory viral infections and are common among children (*1, 2*). The clinical impact of viral coinfections is unclear: while some studies indicate that coinfections do not alter the outcome of disease (*3-5*), others report increased incidence of viral pneumonia (*6, 7*). At the cellular level, the underlying interactions that determine the outcome of coinfections are unclear. Direct interactions between viruses within coinfected cells can result in changes to viral progenies, including -but not limited to- pseudotyping (incorporation of surface proteins from a different virus) (*8-10*) or genomic rearrangements, which may generate novel strains with pandemic potential such as SARS-CoV-2 and pandemic influenza A viruses (*11, 12*). Here, we examined interactions between two commonly co-circulating viruses of clinical importance: influenza A virus (IAV) and respiratory syncytial virus (RSV). IAV causes over five million hospitalizations each year (*13*) and RSV is the leading cause of acute lower respiratory tract infection in children under five years of age (*14, 15*).

To study virus-virus interactions during confection, we infected a cell line derived from human lung (A549) (*16*), with a mixed inoculum of IAV and RSV, or individual viruses as controls. Infections were performed at high multiplicity of infection (MOI) to facilitate coinfection and recapitulate high MOIs produced in advanced stages of infection (when IAV and RSV foci may come into contact). We compared viral replication in single infections and coinfections. Single IAV infections resulted in robust replication, peaking between 24-48 hours post-infection (hpi). In coinfections, IAV replication was similar to that observed in coinfection or at some timepoints marginally increased (Fig. 1a, top left). As RSV titres peaked in single infections at a later timepoint than IAV (72 hpi, Fig. 1a, top right), further infections were performed to determine optimal conditions for coinfections by using a reduced IAV MOI (ten-fold reduction relative to RSV). The reduced IAV input did not affect IAV replication, which still replicated to higher titres in coinfections (Fig. 1a, bottom left). In contrast, RSV titres were significantly reduced, by over 400-fold at 72 hpi, in the presence of IAV both at equivalent MOI (Fig. 1a, top right) and when IAV MOI was reduced relative to RSV (Fig. 1a, bottom right). These results are consistent with published studies that show that RSV is adversely impacted by coinfection, while IAV replication is not (*17, 18*).

To assess if coinfection affected localization of key viral proteins or the proportion of infected cells, single and coinfections were performed as described above and cells were fixed at 24 hpi. Immunofluorescence microscopy revealed that cells infected with either RSV or IAV displayed features typical of the replicative cycle of each virus, such as cytoplasmic inclusion bodies containing RSV nucleoprotein (N), or diffuse IAV nucleoprotein (NP) staining within the cytoplasm (Fig. 1b, left column). Similar features were observed in coinfected cells (Fig. 1b, boxed area) suggesting that coinfection did not affect the intracellular localization of viral proteins. We counted the number of infected cells in single infections alongside the number of single infected and coinfected cells in the coinfection condition. We observed a high proportion of coinfected cells at 24 hpi when cells were infected with equivalent amounts of virus as well as when IAV input MOI was reduced 10-fold relative to RSV (Fig. 1c), suggesting that superinfection exclusion does not prevent coinfection. Paradoxically, a higher number of RSV-positive cells were detected in coinfections than in RSV single-infected samples, contrasting with the observed reduction in RSV titre in coinfections.

IAV and RSV are enveloped viruses that target lipid rafts for assembly and budding (*19, 20*). We therefore stained cells for the major glycoproteins of IAV and RSV: hemagglutinin (HA) and RSV fusion (F), respectively (Fig. 1b, right column) and examined their localisation at plasma membranes. IAV HA diffusely coated the plasma membrane of infected cells in both single virus infections and coinfections, while RSV F was localized to regions containing filamentous structures extending from the cell surface, corresponding to budding RSV virions. In coinfected cells, HA was not excluded from RSV budding sites (Fig. 1b, right column, boxed area). We thus hypothesized that mixing of glycoproteins within these regions may result in incorporation of both IAV and RSV components to budding viral particles. To test this, we applied super-resolution confocal microscopy to image virions immunolabelled for HA and F at high resolution. We observed dual-positive fluorescence suggesting the presence of budding viral filaments possessing both IAV and RSV glycoproteins during coinfection (Fig. 2a, b). Strikingly, minimal colocalization between the two glycoproteins was observed. Instead, glycoproteins were incorporated in distinct regions along the filament, with most dual-positive filaments positive for IAV HA at the distal end (Extended Data Fig. 1). 56±9.1% (mean ± SD) of coinfected cells displayed cell-associated dual-positive filaments. Many of these cells showed extensive production of dual-positive filaments, with no obvious indication of cell damage (Fig. 2c, d). We also observed dual-positive filaments distant from coinfected cells, suggesting they remained intact upon budding (Fig. 2b). Nested among dual-positive filaments (both cell-associated and released), we identified filaments corresponding to IAV and RSV virions (identified by HA or F only staining) (Fig. 2a, b, Extended Data Fig. 1). This indicates

that regions in which dual-positive filaments form may contain both IAV and RSV budding sites.

We performed microscopy on live cells to visualize the native organization of the filaments budding from coinfected cells. Consistent with our previous observations, we detected bundles of filaments protruding from the cell surface that incorporated F along the length of the filament with HA localized at the distal end (Fig. 2e). To obtain better resolution of these budding viruses, we used scanning electron microscopy (SEM). IAV single infection revealed a pleomorphic population of membrane-associated structures consistent with spherical, bacilliform and filamentous particles, whereas RSV single infection resulted in dense clusters of budding RSV filaments (Extended Data Fig. 2). In coinfected cells we identified RSV–like filaments with structures branching from the distal ends resembling smaller bacilliform IAV-like virions (Fig. 2f).

To determine the structural details of IAV/RSV filamentous structures budding from coinfected cells, we performed cryo-electron tomography (cryo-ET) and observed structures consistent with hybrid viral particles containing elements of both IAV and RSV. We repeatedly observed two classes of hybrid particles with some virions exhibiting features of both classes: in 11 cryo-tomograms we observed true hybrid virus particles (HVPs, Fig. 3), and in 16 cryo-tomograms we observed pseudotyped viruses (PVs, Extended data Fig. 3). Pleomorphic IAV particles and RSV filaments were also identified (Extended data file 1, Extended Data Movies 1-2).

HVPs exhibited distinct IAV-like and RSV-like structural regions: the wider part of the filament resembled RSV and extended continuously towards the distal end to one or more narrow, IAV-like regions (Fig. 3a-b, Extended data Fig. 4, Movies 1 and 2). Density consistent with both IAV and RSV ribonucleoproteins (RNPs) could be visualized and seemed confined within their respective structural regions of the filaments (*21, 22*) (Fig. 3a, b and d). Glycoproteins consistent in size, shape and density with IAV or RSV glycoproteins decorated the respective IAV or RSV-like regions of the particles (Fig. 3c and e). In some virions, the junction between IAV and RSV regions had a clear lumen (Extended Data Fig. 4c, Movie 2), whilst other particles exhibited a much narrower join, with pinching off membranes between IAV and RSV areas (Fig. 3f, Movie 1, Extended Data Fig. 4a). Matrix layers were observed in IAV and RSV regions but were absent from the membrane bridging the two regions (Fig. 3f).

We also identified virions consistent with RSV filaments containing (containing RSV RNPs) that had a different glycoprotein ordering than expected (Extended data Fig. 3). The glycoproteins differed in shape when compared to those present on RSV virions and had a

triangular arrangement which resembled IAV glycoproteins (Extended data fig. 3c), rather than ring shaped density more consistent with RSV glycoproteins (Extended data fig. 3e). They also lacked the long-range helical ordering typical of RSV glycoproteins (Extended data fig.3c and e) (*23*). We designated these structures *pseudotyped viruses* (Extended Data Fig. 3a, c and d, Movie 3). Some HVPs with distinct IAV- and RSV-like structural regions also exhibited pseudotyping within the RSV region (Extended Data Fig. 4a-b). Notably, we did not observe IAV virions or IAV-like regions in hybrid particles that were pseudotyped with RSV glycoproteins. To quantify differences in glycoprotein arrangement, we determined the inter-spike distance on IAV, RSV and PVs. RSV exhibited a mean (+/- SD) inter-spike spacing of 12.9 (+/-2.32) nm, while IAV had a spacing of 8.71 (+/-1.18) nm. PVs had an average spike distance ranging from 8.31-9.56 nm, similar to IAV but significantly different to RSV ($p<0.0001$, unpaired t-test) (Extended Data Fig. 5). These results confirm that coinfections can result in the formation of two classes of hybrid viral particles structurally distinct from either parental virus.

As surface glycoproteins determine antigenicity and tropism, and HVPs incorporate glycoproteins of both IAV and RSV, we hypothesized that HVPs would display altered antigenicity. To test this, we first compared the neutralization efficiency of anti-IAV hemagglutinin (HA) antibodies against viruses collected from cells infected with IAV alone, or coinfected with IAV and RSV. As RSV is predominantly cell-associated, we performed neutralization assays using supernatant and cell-associated fractions (see methods). Viruses were also back-titrated to determine infectious titre of the inoculum (Extended data Fig. 6) Viruses collected from coinfected cells displayed reduced IAV neutralization compared to those collected from single IAV infections (Fig 4a). While the observed differences were not statistically significant, the decrease in neutralization efficiency was more marked in the cell-associated fraction of the coinfected cells (Fig. 4a) where only 33% (+/- 27%) (mean [+/- SD]) of IAV was neutralized, suggesting that two-thirds of IAV within this fraction was able to evade antibody-mediated neutralization (Fig. 4a). In an analogous experiment, we compared the neutralization efficiency of anti-RSV F antibodies (Palivizumab) against viruses collected from cells infected with RSV alone or coinfected. RSV harvested from both single and mixed infections was efficiently neutralized (Fig. 4b). This suggests that, in contrast to IAV, RSV cannot utilise IAV glycoproteins to facilitate viral entry. Further, in the context of PVs, RSV infectivity may be determined by the ratio of incorporated IAV and RSV glycoproteins, where fully pseudotyped RSV filaments may be non-infectious, as they are unable to utilise IAV HA.

166 To determine if the incorporation of RSV glycoproteins could result in an expansion of IAV
167 receptor tropism, we treated cells with neuraminidase (NA) to remove sialic acids (the cellular
168 receptor for IAV) (Extended Data Fig. 7a). Sialic acid removal was confirmed by lectin staining
169 (Extended Data Fig. 7b). Virus was harvested from IAV or RSV single infections or
170 coinfections as described for neutralisation assays and subsequently used to inoculate IAV-
171 receptor-deficient (NA-treated) or control cells (Fig. 5a), as well as being back-titrated to
172 determine the IAV titre in the inoculum (Extended data Fig. 7c). Cells were fixed at 12 hpi,
173 immunostained for IAV NP or RSV N and infected cells quantified. IAV entry was blocked in
174 NA-treated cells when inoculated with the released virus of single IAV-infected cells, whereas
175 entry of cell-associated IAV collected from single IAV infections was reduced by 90% (Fig.
176 5a). When NA-treated cells were inoculated with released or cell-associated virus harvested
177 from mixed infections, IAV entry was significantly increased compared to IAV-only infection
178 (Fig. 5a). The increase in IAV entry was higher in the cell-associated fraction, and IAV entry
179 in receptor-deficient cells was restored to 63% (+/- 10%) (mean [+/- SD]) of the level of control
180 cells (Fig. 5a). As RSV does not use sialic acids as receptors, no differences in RSV entry
181 between NA-treated or control cells were detected (Extended Data Fig. 7d). To determine if
182 extracellular association between free IAV and RSV virions was contributing to IAV entry in
183 NA-treated cells, IAV and RSV were mixed and incubated prior to infecting NA-treated or
184 control cells. No significant differences were observed in IAV or RSV entry into receptor-
185 deficient cells compared to control cells when the viruses had been pre-mixed (Extended data
186 Fig. 7e), compared to each virus alone, suggesting that IAV and RSV do not associate upon
187 extracellular mixing or that association does not impact viral entry. Overall, our findings
188 suggest that the increase in IAV entry to sialic acid-deficient cells was a result of hybrid particle
189 formation and indicate that HVPs represent a subpopulation of infectious virus particles with
190 expanded receptor tropism. To determine whether the expansion of IAV tropism was mediated
191 by the RSV F glycoprotein, virus harvested from mixed infections was incubated with
192 Palivizumab. We observed a significant reduction in entry of both released and cell-associated
193 IAV into NA-treated cells in the presence of Palivizumab (Fig. 5b-c), suggesting that RSV F
194 facilitates IAV infection via hybrid particles that enable IAV to enter cells that would otherwise
195 be refractory to infection. We measured IAV entry into untreated control cells (i.e. cells with
196 normal expression of sialic acids) in the presence or absence of Palivizumab. We observed that
197 in the presence of Palivizumab, entry of IAV harvested from the cell associated fraction of
198 coinfections was reduced by approximately half, compared to the Palivizumab-free control
199 (Fig. 5d). This suggests that there is a population of IAV that is dependent on RSV F to gain

200 entry to cells, which in turn suggests that RSV F is the functional glycoprotein of IAV/RSV
201 HVPs.

202 Our cryo-ET data showed that HVPs contain IAV and RSV genomes. To determine if they
203 possess infectivity for both viruses, we infected NA-treated cells with virus harvested from
204 single or mixed infections. At 12 hpi, cells were fixed and stained for IAV HA and RSV F and
205 imaged by confocal microscopy. The presence of coinfected cells suggested that both genomes
206 were delivered into the cells simultaneously, likely by HVPs (Fig. 6a-b). This conclusion is
207 based on the facts that 12 hours is not a sufficiently long time to allow extensive cell-to-cell
208 spread by IAV and RSV which may result in coinfection; and because the probability of
209 coinfection by chance was low as the MOI for each virus was approximately 0.01 (based on
210 back-titrations of harvested virus). Examination of coinfected cells using super-resolution
211 microscopy revealed viral IAV HA and RSV F double-positive filaments (Fig. 6b), suggesting
212 that the HVPs can be maintained over virus passage. To establish if HVPs could spread IAV
213 from cell to cell within a population of cells refractory to IAV infection, we infected NA-treated
214 or control cells with virus harvested from IAV single infections or from the cell-associated
215 fraction of mixed infections (the fraction with enriched HVPs). We then applied an overlay to
216 prevent virion diffusion and incubated the cells for 48 hours. As expected, in single IAV
217 infections, abundant IAV-positive cells were observed in non-treated cells (Fig. 6c, top row).
218 In the NA-treated cells, no infection by IAV from single infections was observed (Fig. 6c,
219 middle row), whereas IAV foci consisting of multiple distinct infected cells were observed in
220 NA-treated cells infected with virus from mixed infections (Fig. 6c, bottom row). Notably,
221 IAV-positive foci colocalised with RSV-positive foci (Fig. 6c, bottom row). These results
222 suggests that HVPs can mediate the spread of IAV within a refractory cell population.

223 To determine the potential for HVP formation in a more biologically relevant system, we
224 coinfected differentiated primary human bronchial epithelial cells (HBECs). We observed no
225 difference in IAV replication kinetics between single-infected and coinfected cultures (Fig. 7a).
226 In coinfections, RSV titres were variable, but the average titres over experimental replicates
227 were lower than in single infections (Fig. 7b). Trends in replication kinetics between single and
228 mixed infections matched the trends observed in A549 cells, providing confidence that viral
229 interactions are conserved between the two systems. To examine the spread of IAV and RSV
230 in HBECs, we fixed and paraffin-embedded infected or mock-infected cultures (culture
231 morphologies shown in Fig. 7c), and performed immunostaining using antibodies targeting
232 IAV HA, IAV NP and a polyclonal antibody raised against the whole RSV virion. We observed
233 diffuse staining for IAV HA and RSV across the apical layer of cells in single infections,

234 whereas in coinfected cultures there was a high degree of individual cells infected by each virus
235 as well as evidence of coinfected cells (Fig. 7d). Analysis of individual coinfected cells
236 revealed dual staining for both IAV and RSV antigens both at the apical surface of coinfected
237 cells and within the cytoplasm (Fig. 7e-f), providing an opportunity for interactions between
238 IAV and RSV and the formation of HVPs.

239 **Discussion**

240 Respiratory viruses share a common tropism for the human respiratory tract and cause
241 significant disease burden. While there is increasing evidence that interactions amongst viruses
242 play an important role on virus dynamics and transmission, most of what is known about virus
243 biology and pathogenesis is based on a tractable but reductionist research approach whereby
244 each virus is studied in isolation.

245 Recent work provided evidence that interactions among respiratory viruses occur and have
246 measurable outcomes at multiple levels, from populations, to individuals and tissues (*24-28*).
247 However, studies characterizing direct virus-virus interactions within cells are scarce. Here we
248 describe previously unknown interactions between IAV and RSV, two clinically important
249 respiratory viruses that belong to different taxonomical families.

250 We show that, in coinfections IAV replicates to equivalent or marginally higher titres compared
251 to single IAV infections, whereas RSV replication is reduced. The consistency in IAV
252 replication kinetics in the presence or absence of RSV contrasts with the inhibition of IAV
253 replication in coinfections with rhinovirus (*26*). This indicates that the consequences of
254 coinfections are highly dependent on the viruses involved as they trigger virus-specific cellular
255 responses.

256 We also show compelling evidence that coinfections can generate infectious HVPs composed
257 of structural, genomic, and functional components of both parental viruses. As HVPs can evade
258 IAV-targeted neutralisation and infect cells lacking IAV receptors suggests that coinfections
259 can generate viruses with altered antigenicity and expanded tropism. Using Palivizumab, we
260 showed that RSV F mediates HVP entry, indicating that in the context of a hybrid particle, IAV
261 can use the glycoprotein of an unrelated virus as its functional envelope protein. This property
262 may facilitate within-host dissemination to areas of the respiratory tract that are refractory to
263 infection by one of the parental viruses, which is likely to impact pathogenesis and disease
264 outcome. For example, IAV predominantly infects the upper and middle respiratory tract
265 causing uncomplicated influenza, while RSV spreads more readily to the middle and lower
266 respiratory tract (LRT) (*29, 30*). HVPs could enable IAV to escape mucosal antibodies while

spreading to the LRT, with subsequent potential complications, including viral pneumonia (*30*). In addition, as IAVs exhibit high mutation rates, LRT infections by HVPs might favor the selection of IAVs with increased tropism for the LRT and therefore result in selection of more pathogenic viruses.

In recent years, a novel conceptual framework that incorporates social evolution theory has been developed to explain how virus-virus interactions can play an important role on virus function and fitness (*31*). We show that HVP formation is maintained over multiple rounds of infection and that HVPs facilitate the spread of IAV within a population of refractory cells. This observation aligns with the concept that, like other pathogens and organisms, viruses can engage in social-like traits, that are beneficial to virus fitness and function.

Using a lung-derived human cell line, we show that the generation of HVPs by coinfection is biologically feasible. The fact that IAV and RSV cocirculate in winter in the same populations (*1*), have a shared tropism for ciliated epithelial cells (*32, 33*), bud from the apical cellular surface (*22, 33, 34*) and coinfect cells within the respiratory epithelium (this work) suggest that HVPs have the potential to be generated *in vivo*. The likelihood of a cell becoming coinfected during natural infection remains unknown but will vary depending on the timing of infection and the localization of infectious foci within the respiratory tract. Estimates of viral bursts show that as viral load increases, the effective MOI to susceptible cells surrounding an infectious focus increases (*35*), enhancing the probability of cellular coinfection and therefore the potential generation of HVPs.

The formation of HVPs raises questions about fundamental rules that govern viral assembly and budding. These processes, which are thought to be highly regulated, involve selective recruitment, trafficking (*36, 37*) and multimerization of viral proteins (*19, 38-40*) within specific compartments of the cell. While we described the formation of HVPs as a consequence of coinfection by IAV and RSV, we hypothesize that coinfections involving other pleomorphic enveloped viruses are also likely to generate HVPs. However, we pose that formation of infectious HVPs requires more than structural compatibility, and includes similar tropism, absence of superinfection exclusion or interference, as well as seasonal and geographical co-circulation. RSV is a pleomorphic enveloped virus with a broad tropism for different regions of the respiratory tract and is frequently observed in co-infections in winter (*41-43*) , therefore RSV is a good candidate to form HVPs with other respiratory viruses. This might explain some of the mechanisms that lead to viral pneumonia (*44*). Further studies will be required to address which virus combinations can generate infectious HVPs; which viral properties favor their formation; and how they impact on pathogenesis and virus transmission.

301 **Online Methods**

302 **Cells**

303 Human lung adenocarcinoma cells (A549) (American Type Culture Collection [ATCC], CCL-
304 185), Madin Darby canine kidney (MDCK) cells (ATCC, CCL-34) and HEp-2 (ATCC, CCL-
305 23) cells were cultured in Dulbecco's Minimum Essential Media (DMEM), high glucose,
306 GlutaMAX supplemented with 10% fetal bovine serum (FBS).

307 Human bronchial epithelial cells (hBEC) were cultured and differentiated at air-liquid interface
308 as describe previously (*24*). Briefly, human bronchial epithelial cells (hBEC) (Epithelix,) were
309 cultured in Epithelix human airway epithelial cell medium (Epithelix; EP09AM) 37˚c, 5% CO2
310 in a humidified incubator. Cells were cultured in tissue culture flasks until 80% confluent. After
311 this point, cells were trypsinised and seeded at $2x10^4$ cells/transwell onto transwell inserts for
312 24-well plate with 0.4 µm pore size with a pore density of $1.6x10^6$ pores per cm2 (Falcon, 734-
313 0036). When cells were fully confluent on transwell membranes, apical media was removed to
314 initiated air-liquid interface (ALI). Basal media was replaced with Pneumacult-ALI media
315 (STEMCELL Technologies, 05001). Basal media was replenished every 2-3 days. When
316 cultures began producing mucus (approximately 20 days post ALI initiation), the apical surface
317 of cultures was washed twice weekly with serum free DMEM.

318 **Viruses**

319 H1N1 influenza A/Puerto Rico/8/34 was rescued as previously described (*45*) and virus stocks
320 were grown in MDCK cells. RSV strain A2 (American Type Culture Collection, VR-1540)
321 was grown in HEp-2 cells.

322 **Antibodies**

323 The following primary antibodies were used at optimised concentrations: RSV fusion
324 glycoprotein (Abcam, UK, AB24011, 1/1000), RSV nucleoprotein (Abcam, UK, AB22501,
325 1/1500), antisera to influenza A H1 (A/Puerto Rico/8/34, 1/1000) (NIBSC, UK, 03/242),
326 influenza A virus nucleoprotein (European Veterinary Society, EVS238, 1/1000), mouse
327 monoclonal anti-IAV (A/Puerto Rico/8/34) HA (Sinobiological, 11684-MM03, 1/500),
328 polyclonal anti-IAV (A/Puerto Rico/8/34) nucleoprotein kindly provided by Paul Digard, goat
329 polyclonal anti-RSV (Abcam, AB20745, 1/500) Secondary antibodies: Rabbit anti-mouse IgG
330 alexafluor 488 conjugate (Sigma-Aldrich, USA, SAB4600056, 1/1000), donkey anti-mouse
331 594 conjugate (Abcam, UK, ab150108, 1/1000) donkey anti-sheep alexafluor 594 conjugate

332 (Thermo Fisher Scientific, USA, A-11016, 1/1000),), goat anti-rabbit alexafluor 488
333 (Invitrogen, A11034).

334 **Virus growth curves**

335 A549 cells were infected with IAV, RSV or synchronously infected with a mixed inoculum of
336 IAV and RSV, diluted in DMEM, with 2% FBS and 1µg/ml trypsin TPCK. Infections were
337 carried out with RSV at a multiplicity of infection (MOI) of 4 and IAV at an MOI of 4 or 0.4.
338 A549 cells were inoculated in 48-well plates and incubated at 37˚C, 5% CO2 for 90 minutes,
339 before the inoculum was removed and replaced with DMEM, with 2% FBS and 1µg/ml trypsin
340 TPCK. Cells were incubated at 37˚C, 5% CO2 and supernatant from each infection was
341 collected at 24, 48 and 72 hours post infection and stored at -80˚C prior to titration by plaque
342 assay.

343 HBEC cultures were infected no earlier than 35 days post ALI initiation. The apical surface of
344 cultures was washed with DMEM 24 hours prior to infection by applying pre-warmed DMEM
345 to the apical surface of cultures and incubating at 37˚c, 5% CO2 in a humidified incubator for
346 20 minutes, followed by removal. This washing step was repeated immediately before
347 infection. Inoculum containing 105 pfu of IAV, RSV or a mixed inoculum of both viruses (105
348 pfu of each virus) was prepared in DMEM. Cultures were incubated with inoculum for 2 hours
349 at 37˚c 5% CO2, after which the inoculum was removed and cultures were washed once with
350 DMEM as described. Inoculum was back titrated back plaque assay to confirm virus input and
351 served as the zero hours time point for growth curves. Two cultures were infected per infection
352 condition and experimental time point. Samples were collected from the apical surface of
353 cultures at 24, 48 and 72 hpi, by incubating with DMEM for 30 minutes. Sample were then
354 removed and stored at -80˚c, prior to titration by IAV or RSV plaque assay. Transwells were
355 fixed with 4% formaldehyde for 1 hour. After fixation, HBEC cultures were embedded in
356 paraffin blocks, cut to 2-3 µm thick sections and mounted on glass slides. Sections were stained
357 with haematoxylin and eosin to determine morphology.

358 Infectious titre was determined by plaque assay in MDCK cells or HEp-2 cells for IAV and
359 RSV, respectively. Validation was carried out prior to these experiments to ensure specific
360 detection of IAV or RSV plaques in the respective cell type. While IAV and RSV are capable
361 of infecting both cell lines, each cell line is only permissive to plaque formation by one virus
362 I.e. IAV forms plaques in MDCK but not HEp-2cells, while RSV forms plaques in HEp-2 but
363 not MDCK cells. Viruses were titrated in 10-fold serial dilutions in duplicate and incubated on
364 confluent cell monolayers for 90 minutes. For IAV plaque assays, overlay containing DMEM,

365 1µg/ml trypsin TPCK and 0.6% Avicel was used and plates were incubated at 37˚C, 5% CO2
366 for 48 hours. For RSV plaque assays, overlay containing DMEM, 5% FBS and 0.6% Avicel
367 was applied and plates were incubated at 37˚C, 5% CO2 for 4-5 days. Plates were then fixed
368 with 4% formaldehyde in phosphate buffered solution (PBS) and stained with 0.1% Coomassie
369 Brilliant Blue. Plaques were counted and titre determined as plaque forming units per ml
370 (pfu/ml). Experiments were carried out in technical (n=3) and biological triplicate (n=3
371 independent experiments).

372 **Immunofluorescence and confocal microscopy**

373 Cells were seeded at $2x10^5$ cells/ml on 13 mm glass coverslips or 35mm glass bottom dishes
374 (MATTEK Corporation Inc, USA) prior to infection. Infections were incubated for 24 hours
375 prior to fixation with 4% fomaldehyde in PBS. Fixed cells were permeabilized with 0.1%
376 triton X100 for 10 minutes at room temperature. Samples were blocked with 1% bovine serum
377 albumin (BSA) in PBS for 30 minutes. Primary and secondary antibodies were diluted in 1%
378 BSA in PBS and incubated for 60 minutes at room temperature, followed by four washes with
379 PBS. Coverslips were mounted with Prolong Gold mounting media with DAPI (Invitrogen,
380 USA, P36392), and samples in dishes were stained with 2 µg/ml Hoescht 33342 solution for
381 10 minutes. For combining mouse primary antibodies, samples were blocked in rabbit serum
382 (Gentex, USA, GTX73221), then stained with primary antibody and rabbit anti-mouse
383 secondary antibody, followed by secondary blocking in donkey serum (Gentex, USA,
384 GTX73205), then stained with primary antibody and donkey anti-mouse secondary antibody.
385 For live-cell imaging, cells were incubated with 2 µg/ml Hoescht 33342 solution in cell culture
386 media, for 30 minutes at 37˚c. Cells were then washed with cold PBS, followed by incubation
387 with primary antibody diluted in 2% BSA in PBS for 5 minutes on ice. Cells were washed three
388 times with cold PBS and incubated with secondary antibody diluted in 2% BSA in PBS for 5
389 minutes on ice. Cells were stored in PBS and imaged immediately following staining.

390 For immunofluorescence staining, sections were dewaxed by heating in an oven at 60˚c for 1
391 hour. Next, slides were washed four times with xylene, each for 10 minutes. Following this,
392 sections were rehydrated via washes with 1:1 (v/v) Xylene:Isopropanol mixture, then 100%,
393 90%, 70% and 50% isopropyl alcohol solution each for five minutes. Sections were washed
394 thoroughly with d.H_2O and PBS. For antigen retrieval, sections were treated with proteinase K
395 solution (Dako, S3020) for 15 minutes.

396 Sections were mounted into humid chambers for immunostaining. Sections were permeablised
397 with 1% triton X100 for 10 minutes, followed by three washes with PBS. Sections were

398 blocked with 2% BSA in PBS for 30 minutes at room temperature. Primary antibodies were
399 diluted in 2% BSA solution and applied to sections for two hours at room temperature, followed
400 by washing with PBS. Secondary antibodies were diluted in 2% BSA solution and applied to
401 sections for 1 hour in the dark at room temperature, followed washing with PBS and d.H_2O.
402 Slides were mounted with Prolong Gold mounting media containing DAPI (Invitrogen,
403 P36392).

404 Confocal microscopy was carried out using Zeiss LSM880 AxioObserver microscope (ZEISS,
405 Germany). Standard images were collected using GaAsP detector with 405nm, 488nm and
406 598nm excitation lasers, using 40x/1.4 or 63x/1.4 plan-apochromat oil DIC M27 objectives.
407 Super-resolution imaging was collected using the Airyscan detector with 405nm, 488nm and
408 594nm excitation lasers, using plan-apochromat 63x/1.4 oil DIC M27 objective. Z-stacks were
409 collected using a z-interval of 100nm. For determining proportions of infection and focus assay
410 on neuraminidase treated cells, fields of view were imaged using 3x3 tile scans at 40x/1.4 oil
411 DIC M27 objective. Image processing and analysis was carried out in ImageJ software (v2.0.0-
412 rc-56/1.52g) (NIH, USA) and Zeiss Zen lite (Blue edition) version 2.6. Single or coinfected
413 cells were counted manually, using cell counter plugin on ImageJ. Experiments were carried
414 out in technical (n=3) and biological triplicate (n=3 independent experiments).

415 **Scanning electron microscopy**

416 Cells were seeded at $2x10^5$ cells/ml on 13 mm glass coverslips prior to infection at MOI of 4
417 with IAV, RSV or coinfection for 24 hours. Cells were fixed with 1.5% Glutaraldehyde in
418 0.1M Sodium Cacodylate (SC) buffer for 1 hour and washed 3 times for 5 minutes each with
419 0.1M SC buffer before incubation with 1% osmium tetroxide for 1 hour. Samples were then
420 stained with aqueous 0.5% Uranyl Acetate for 1 h and further dehydrated through an ethanol
421 series and subjected to critical point drying using an Autosamdri-815 Critical Point Dryer
422 (Tousimis, USA) before mounting and coating in 20nm Gold/Palladium using a Quorum
423 Q150T ES High vacuum coating system (Quorum Technologies, UK). Images were collected
424 using JEOL IT100 SEM at 20kV, with InTouch Scope software, version 1.05 (JEOL USA Inc.,
425 USA). Infections and imaging were carried out in two independent experiments, with duplicate
426 samples per experiment.

427 **Cryo-electron Tomography and computational analysis**

428 Cells were seeded at $2x10^4$ cells/ml on laminin-coated (Roche) 200-mesh gold R2/2 London
429 finder Quantifoil grids (Electron Microscopy Sciences) in 35 mm glass bottom dishes
430 (MATTEK Corporation Inc, USA). Cells were infected with IAV MOI 1 and RSV MOI 4 and

431 incubated for 24 hours at 37˚C. Cryo-ET imaging experiments of coinfected cells were carried
432 out in three independent experiments, with duplicate grids imaged per experiment. Immediately
433 before plunge-freezing 3 µl colloidal solution of 20 nm gold fiducials (Sigma-Aldrich)
434 pretreated with BSA was added to each grid. The gold served as fiducial markers for cryo-
435 tomogram reconstruction. Grids were blotted from the backside of the grid and plunge-frozen
436 into liquid ethane using the FEI Vitrobot Mark IV (Thermo Fisher Scientific, USA) or Leica
437 EM GP 2 (Leica Microsystems, Germany). Plunge-frozen grids were subsequently loaded into
438 a JEOL CRYO ARM 300 (JEOL Ltd, Japan) equipped with an energy-filter and DE64 detector
439 (Direct Electron, USA). To identify the presence of virus budding sites near electron
440 transparent cellular edges low-magnification grid maps were generated using serialEM (*46*).
441 Next, polygon maps at 3,000x magnification were collected at areas of interest and virus
442 budding sites were identified. Tilt-series of virus budding sites were then recorded using
443 SerialEM at either 30,000x (1.921 Å/pixel) or 50,000x (1.499 Å/pixel) magnification. Each
444 tilt-series was collected from −60° to +60° at an increment of 2° or 3° at 5- to 8-µm underfocus
445 (30,000x) and 2- to 5-µm underfocus (50,000x). The cumulative dose of one tilt-series was
446 between 80 and 120 $e^{-}/Å^{2}$. Tilt-series were collected using a dose-symmetric scheme starting
447 at 0˚ implemented in SerialEM (*47*) and were collected in 'movie mode'. For the 30,000x
448 magnification tilt-series movie frames were aligned using alignframes module in IMOD (*46*).
449 For the 50,000x magnification tilt-series movie frames were aligned using MotionCor2 with 6
450 by 6 patches (*48*). Once tilt-series sub-frames were aligned and binned eightfold into 1 k × 1 k
451 arrays they were reconstructed into 3D tomograms using weighted back projection with IMOD.
452 To aid interpretation and visualization, noise reduction was applied using Topaz (*49*). Figures
453 and supplemental videos were prepared using IMOD, Illustrator ImageJ and Quicktime.
454 Segmentation and isosurface rendering were performed manually using the thresholding tool
455 in Amira (Thermo Fisher Scientific, USA).

456 Glycoprotein-distance was measured and calculated using the imodinfo module in IMOD.
457 Denoised tomograms were averaged between 5-10 slices to improve contrast and glycoproteins
458 were viewed from top down. Distances were measured between the centres of pairs of adjacent
459 glycoproteins. For IAV and RSV controls, spike measurements were collected from 11
460 individual tomograms for each virus (n=326 for IAV, n=236 for RSV). For pseudotyped virus,
461 spike measurements were collected from each particle, from 4 individual tomograms (n=50
462 measurements per tomogram).

463 **Neutralisation assays**

464 A549 cells were seeded at $1x10^5$ cells/well in 24-well plates prior to infection with IAV (MOI
465 of 1), RSV (MOI of 4) or mixed infection. Infected cells were incubated for 24 hours before
466 released virus was harvested from supernatant and cell associated virus was collected by
467 scraping and vortexing infected cells. Virus stocks were back titrated in MDCK or HEp-2 cells
468 to determine pfu/well in the neutralisation assays. For IAV neutralisation assay, IAV from
469 single infection or mixed infection was incubated with polyclonal anti-serum targeting
470 A/Puerto Rico/8/34 H1 (NIBSC, UK, 03/242) at 1/200 dilution in DMEM or a serum-free
471 control. For the RSV neutralisation assay, RSV from single infection or mixed infection was
472 incubated with Palivizumab (Evidentic, Germany) at 10 µg/well concentration diluted in
473 DMEM, or a serum-free control. Virus (neat or at a 1/10 dilution in DMEM) was incubated
474 with serum for 1 hour at 37˚c before transfer to A549 cells that had been seeded at $1x10^4$
475 cells/well in 96-well plates 48 hours prior to infection. Infections were incubated for 12 hours
476 at 37˚c and following this, cells were fixed in 4% fomaldehyde. Plates were
477 immunofluorescence stained for IAV or RSV nucleoprotein and infected cells were quantified
478 using the Celigo automated cytometer (Nexcelom Bioscience, USA), using two target
479 expression analysis. Neutralisation was calculated from the positive cell count in each technical
480 replicate of the serum containing wells as a percentage of the average positive cell count in the
481 serum-free control. Experiments were carried out in biological triplicate (n=3 independent
482 experiments).

483 **Neuraminidase assay**

484 To prepare fresh virus stocks for the neuraminidase assay, A549 cells were seeded at 1x105
485 cells/well in 24-well plates prior to infection with IAV (MOI of 1), RSV (MOI of 4) or mixed
486 infection. Infected cells were incubated for 24 hours before released virus was harvested from
487 supernatant and cell associated virus was collected by scraping and vortexing infected cells.
488 Virus stocks were back titrated in MDCK or HEp-2 cells to determine pfu/well in the
489 neutralisation assays. For the neuraminidase assay, cells were seeded at $1x10^4$ cells/well in 96-
490 well plates, prior to treatment with 1mU/µl neuraminidase from clostridium perfringens
491 (Sigma-Aldrich, USA, N2876) for 2 hours. To confirm removal of sialic acids, neuraminidase
492 treated and control cells were stained with biotinylated Maackia Amurensis Lectin II (MAL II)
493 (Vector Laboratories, UK, B-1265-1), followed by fluorescein conjugated streptavidin (Vector
494 Laboratories, UK, SA-5001-1) or Erythrina Cristagalli Lectin conjugated to fluorescein
495 (Vector Laboratories, UK, FL-1141-5). Neat virus stocks were transferred directly onto
496 neuraminidase treated or untreated cells in 96-well plates or on 13 mm glass coverslips and
497 incubated for 12 hours. Virus harvested from coinfection was also incubated with 10 µg/well

498 Palivizumab for 1 hour at 37˚c, before transfer to NA-treated or untreated control wells and
499 incubated for 12 hours. Cells were fixed and 96-well plates stained for IAV or RSV
500 nucleoprotein, followed by rabbit anti-mouse 488 (Sigma Aldrich, USA, SABA4600056)
501 secondary antibody. Infected cells were counted using Celigo automated cytometer (Nexcelom
502 Bioscience, USA), using two target expression analysis. Viral entry ratio was calculated from
503 the positive cell count in each technical replicate of the NA-treated wells as a percentage of the
504 average positive cell count in the untreated control wells. Fixed coverslips were immunostained
505 for IAV HA or RSV F and imaged by confocal microscopy using Zeiss LSM880 with or
506 without Airyscan detector. Experiments were carried out in biological triplicate (n=3
507 independent experiments).

508 For the focus assay, cells were seeded onto 13 mm glass coverslips at $1x10^5$ cells/well. Cells
509 were treated with 1mU/µl neuraminidase from for 2 hours, before infection with fresh virus
510 stocks harvested from IAV single infection or coinfection or infection of untreated control
511 cells. Infections were overlaid with DMEM containing 0.6% Avicel, 2% FBS and 1 µg/ml
512 trypsin TPCK and incubated at 37˚c for 48 hours. Following this, coverslips were fixed and
513 immunostained for RSV N and IAV HA. Samples were imaged by confocal microscopy using
514 Zeiss LSM880.

515 **Statistical analysis and Data Visualization**

516 Statistical tests were carried out using Graphpad Prism, version 9.1.0. No assumptions about
517 data normality were made and Mann Whitney test was used to determine statistical significance
518 in growth kinetic experiments, neutralisation assays and neuraminidase assays. For inter-spike
519 measurements on tomograms, normal distribution was tested using Shapiro-Wilk test and
520 statistical difference between groups was determined by unpaired t-test. Data was visualised
521 with RStudio version 1.3.1056 (*50*) using GGPlot2 package (*51*). Statistical significance was
522 indicated in figures as ns $p>0.05$, * $p<0.05$, ** $p<0.01$, *** $p<0.001$, **** $p<0.0001$.

523 **References**

524 1. S. Nickbakhsh *et al.*, Extensive multiplex PCR diagnostics reveal new insights into the
525 epidemiology of viral respiratory infections. *Epidemiol Infect* **144**, 2064-2076 (2016).
526 2. A. Franz *et al.*, Correlation of viral load of respiratory pathogens and co-infections with disease
527 severity in children hospitalized for lower respiratory tract infection. *J Clin Virol* **48**, 239-245
528 (2010).
529 3. E. A. Goka, P. J. Vallely, K. J. Mutton, P. E. Klapper, Single and multiple respiratory virus
530 infections and severity of respiratory disease: a systematic review. *Paediatr Respir Rev* **15**,
531 363-370 (2014).
532 4. M. C. Scotta *et al.*, Respiratory viral coinfection and disease severity in children: A systematic
533 review and meta-analysis. *J Clin Virol* **80**, 45-56 (2016).

534 5. S. A. Asner *et al.*, Clinical disease severity of respiratory viral co-infection versus single viral
535 infection: a systematic review and meta-analysis. *PLoS One* **9**, e99392 (2014).
536 6. S. A. Asner, W. Rose, A. Petrich, S. Richardson, D. J. Tran, Is virus coinfection a predictor of
537 severity in children with viral respiratory infections? *Clin Microbiol Infect* **21**, 264 e261-266
538 (2015).
539 7. I. A. Echenique *et al.*, Clinical characteristics and outcomes in hospitalized patients with
540 respiratory viral co-infection during the 2009 H1N1 influenza pandemic. *PLoS One* **8**, e60845
541 (2013).
542 8. J. Zavada, The pseudotypic paradox. *J Gen Virol* **63 (Pt 1)**, 15-24 (1982).
543 9. A. Duverge, M. Negroni, Pseudotyping Lentiviral Vectors: When the Clothes Make the Virus.
544 *Viruses* **12**, (2020).
545 10. R. K. Akkina *et al.*, High-efficiency gene transfer into CD34+ cells with a human
546 immunodeficiency virus type 1-based retroviral vector pseudotyped with vesicular stomatitis
547 virus envelope glycoprotein G. *J Virol* **70**, 2581-2585 (1996).
548 11. M. F. Boni *et al.*, Evolutionary origins of the SARS-CoV-2 sarbecovirus lineage responsible for
549 the COVID-19 pandemic. *Nat Microbiol* **5**, 1408-1417 (2020).
550 12. G. J. Smith *et al.*, Origins and evolutionary genomics of the 2009 swine-origin H1N1 influenza
551 A epidemic. *Nature* **459**, 1122-1125 (2009).
552 13. K. E. Lafond *et al.*, Global burden of influenza-associated lower respiratory tract infections and
553 hospitalizations among adults: A systematic review and meta-analysis. *PLoS Med* **18**,
554 e1003550 (2021).
555 14. H. Nair *et al.*, Global burden of acute lower respiratory infections due to respiratory syncytial
556 virus in young children: a systematic review and meta-analysis. *The Lancet* **375**, 1545-1555
557 (2010).
558 15. T. Shi *et al.*, Global, regional, and national disease burden estimates of acute lower respiratory
559 infections due to respiratory syncytial virus in young children in 2015: a systematic review and
560 modelling study. *The Lancet* **390**, 946-958 (2017).
561 16. G. R. Gaajetaan *et al.*, Interferon-beta induces a long-lasting antiviral state in human
562 respiratory epithelial cells. *J Infect* **66**, 163-169 (2013).
563 17. Y. Drori *et al.*, Influenza A Virus Inhibits RSV Infection via a Two-Wave Expression of IFIT
564 Proteins. *Viruses* **12**, (2020).
565 18. J. A. George, S. H. AlShamsi, M. H. Alhammadi, A. R. Alsuwaidi, Exacerbation of Influenza A
566 Virus Disease Severity by Respiratory Syncytial Virus Co-Infection in a Mouse Model. *Viruses*
567 **13**, (2021).
568 19. J. S. Rossman, R. A. Lamb, Influenza virus assembly and budding. *Virology* **411**, 229-236 (2011).
569 20. L. H. McCurdy, B. S. Graham, Role of plasma membrane lipid microdomains in respiratory
570 syncytial virus filament formation. *J Virol* **77**, 1747-1756 (2003).
571 21. S. Vijayakrishnan *et al.*, Cryotomography of budding influenza A virus reveals filaments with
572 diverse morphologies that mostly do not bear a genome at their distal end. *PLoS Pathog* **9**,
573 e1003413 (2013).
574 22. Z. Ke *et al.*, The Morphology and Assembly of Respiratory Syncytial Virus Revealed by Cryo-
575 Electron Tomography. *Viruses* **10**, (2018).
576 23. M. J. Conley *et al.*, Helical ordering of envelope-associated proteins and glycoproteins in
577 respiratory syncytial virus. *EMBO J* **41**, e109728 (2022).
578 24. K. Dee *et al.*, Human rhinovirus infection blocks SARS-CoV-2 replication within the respiratory
579 epithelium: implications for COVID-19 epidemiology. *J Infect Dis*, (2021).
580 25. S. Nickbakhsh *et al.*, Virus-virus interactions impact the population dynamics of influenza and
581 the common cold. *Proc Natl Acad Sci U S A*, (2019).
582 26. A. Wu, V. T. Mihaylova, M. L. Landry, E. F. Foxman, Interference between rhinovirus and
583 influenza A virus: a clinical data analysis and experimental infection study. *Lancet Microbe* **1**,
584 e254-e262 (2020).
585 27. N. R. Cheemarla *et al.*, Dynamic innate immune response determines susceptibility to SARS-
586 CoV-2 infection and early replication kinetics. *J Exp Med* **218**, (2021).

587 28. S. D. Meskill, P. A. Revell, L. Chandramohan, A. T. Cruz, Prevalence of co-infection between
588 respiratory syncytial virus and influenza in children. *The American Journal of Emergency*
589 *Medicine* **35**, 495-498 (2017).
590 29. J. E. Johnson, R. A. Gonzales, S. J. Olson, P. F. Wright, B. S. Graham, The histopathology of fatal
591 untreated human respiratory syncytial virus infection. *Mod Pathol* **20**, 108-119 (2007).
592 30. T. Kuiken, J. K. Taubenberger, Pathology of human influenza revisited. *Vaccine* **26 Suppl 4**,
593 D59-66 (2008).
594 31. S. L. Diaz-Munoz, R. Sanjuan, S. West, Sociovirology: Conflict, Cooperation, and
595 Communication among Viruses. *Cell Host Microbe* **22**, 437-441 (2017).
596 32. K. P. Hui *et al.*, Tropism, replication competence, and innate immune responses of influenza
597 virus: an analysis of human airway organoids and ex-vivo bronchus cultures. *The Lancet*
598 *Respiratory Medicine* **6**, 846-854 (2018).
599 33. L. Zhang, M. E. Peeples, R. C. Boucher, P. L. Collins, R. J. Pickles, Respiratory syncytial virus
600 infection of human airway epithelial cells is polarized, specific to ciliated cells, and without
601 obvious cytopathology. *J Virol* **76**, 5654-5666 (2002).
602 34. L. Kolesnikova *et al.*, Influenza virus budding from the tips of cellular microvilli in differentiated
603 human airway epithelial cells. *J Gen Virol* **94**, 971-976 (2013).
604 35. L. Mohler, D. Flockerzi, H. Sann, U. Reichl, Mathematical model of influenza A virus production
605 in large-scale microcarrier culture. *Biotechnol Bioeng* **90**, 46-58 (2005).
606 36. E. A. Bruce, P. Digard, A. D. Stuart, The Rab11 pathway is required for influenza A virus budding
607 and filament formation. *J Virol* **84**, 5848-5859 (2010).
608 37. T. J. Utley *et al.*, Respiratory syncytial virus uses a Vps4-independent budding mechanism
609 controlled by Rab11-FIP2. *Proc Natl Acad Sci U S A* **105**, 10209-10214 (2008).
610 38. D. S. Lyles, Assembly and budding of negative-strand RNA viruses. *Adv Virus Res* **85**, 57-90
611 (2013).
612 39. P. Chlanda *et al.*, Structural Analysis of the Roles of Influenza A Virus Membrane-Associated
613 Proteins in Assembly and Morphology. *J Virol* **89**, 8957-8966 (2015).
614 40. G. Kiss *et al.*, Structural analysis of respiratory syncytial virus reveals the position of M2-1
615 between the matrix protein and the ribonucleoprotein complex. *J Virol* **88**, 7602-7617 (2014).
616 41. Y. Li, P. Pillai, F. Miyake, H. Nair, The role of viral co-infections in the severity of acute
617 respiratory infections among children infected with respiratory syncytial virus (RSV): A
618 systematic review and meta-analysis. *J Glob Health* **10**, 010426 (2020).
619 42. C. Calvo *et al.*, Respiratory Syncytial Virus Coinfections With Rhinovirus and Human Bocavirus
620 in Hospitalized Children. *Medicine (Baltimore)* **94**, e1788 (2015).
621 43. L. M. Yoshida *et al.*, Respiratory syncytial virus: co-infection and paediatric lower respiratory
622 tract infections. *Eur Respir J* **42**, 461-469 (2013).
623 44. O. Ruuskanen, E. Lahti, L. C. Jennings, D. R. Murdoch, Viral pneumonia. *Lancet* **377**, 1264-1275
624 (2011).
625 45. C. T. Benfield, J. W. Lyall, G. Kochs, L. S. Tiley, Asparagine 631 variants of the chicken Mx
626 protein do not inhibit influenza virus replication in primary chicken embryo fibroblasts or in
627 vitro surrogate assays. *J Virol* **82**, 7533-7539 (2008).
628 46. J. R. Kremer, D. N. Mastronarde, J. R. McIntosh, Computer visualization of three-dimensional
629 image data using IMOD. *J Struct Biol* **116**, 71-76 (1996).
630 47. D. N. Mastronarde, Automated electron microscope tomography using robust prediction of
631 specimen movements. *J Struct Biol* **152**, 36-51 (2005).
632 48. S. Q. Zheng *et al.*, MotionCor2: anisotropic correction of beam-induced motion for improved
633 cryo-electron microscopy. *Nat Methods* **14**, 331-332 (2017).
634 49. T. Bepler, K. Kelley, A. J. Noble, B. Berger, Topaz-Denoise: general deep denoising models for
635 cryoEM and cryoET. *Nat Commun* **11**, 5208 (2020).
636 50. R. C. Team, R: A language and environment for statistical computing. (2013).
637 51. H. Wickham, Elegant graphics for data analysis. *Media* **35**, 10.1007 (2009).
638 52. L. J. Calder, S. Wasilewski, J. A. Berriman, P. B. Rosenthal, Structural organization of a
639 filamentous influenza A virus. *Proc Natl Acad Sci U S A* **107**, 10685-10690 (2010).

640 53. D. Bhella, A. Ralph, L. B. Murphy, R. P. Yeo, Significant differences in nucleocapsid morphology
641 within the Paramyxoviridae. *J Gen Virol* **83**, 1831-1839 (2002).

642 **Data Availability**

643 Representative tomograms of the chimeric virus particles described in this paper have been
644 deposited in the Electron Microscopy Data Bank (www.ebi.ac.uk/emdb) under accession codes
645 EMD-13228 and EMD-13229.

646 **Author contributions.**

647 Author contributions are based on the CRediT taxonomy (https://casrai.org/credit/). J.H.:
648 Investigation, Methodology, Formal analysis, Visualisation, Writing - original draft; S.V.:
649 Investigation, Data curation, Formal analysis, Resources, Metodology, Validation,
650 Visualisation, Supervision Writing- original draft; J.S.: Investigation, Writing – review and
651 editing; K.D.: Investigation, Writing – review and editing; D.M.G.: Investigation, Writing –
652 review and editing; M.C.: Investigation, Writing – review and editing; M.M.: Investigation,
653 Methodology, Writing – review and editing; S.D.C: Formal analysis, writing, review and
654 editing; D.B.: Resources, Funding acquisition, Writing – review and editing; P.R.M.:
655 Conceptualization, Methodology, Validation, Data curation, Supervision, Funding acquisition,
656 Project administration, Writing – original draft.

657 **Acknowledgments**

658 This work was supported by grants from the Medical Research Council of the United Kingdom
659 (MC_UU_12014/9 to PRM, MR/N013166/1 to JH, MR/R502327/1 to DMG,
660 MC_UU_12014/7 to SV, and MC_UU_12014/7 to DB). The Scottish Centre for
661 Macromolecular Imaging (SCMI) is funded by the MRC (MC_PC_17135) and SFC (H17007).

662 **Conflicts of interest.** The authors declare no conflicts of interest.

663 Correspondence and requests for materials should be addressed to Pablo Murcia.

664 Reprints and permissions information is available at www.nature.com/reprints.

Figures

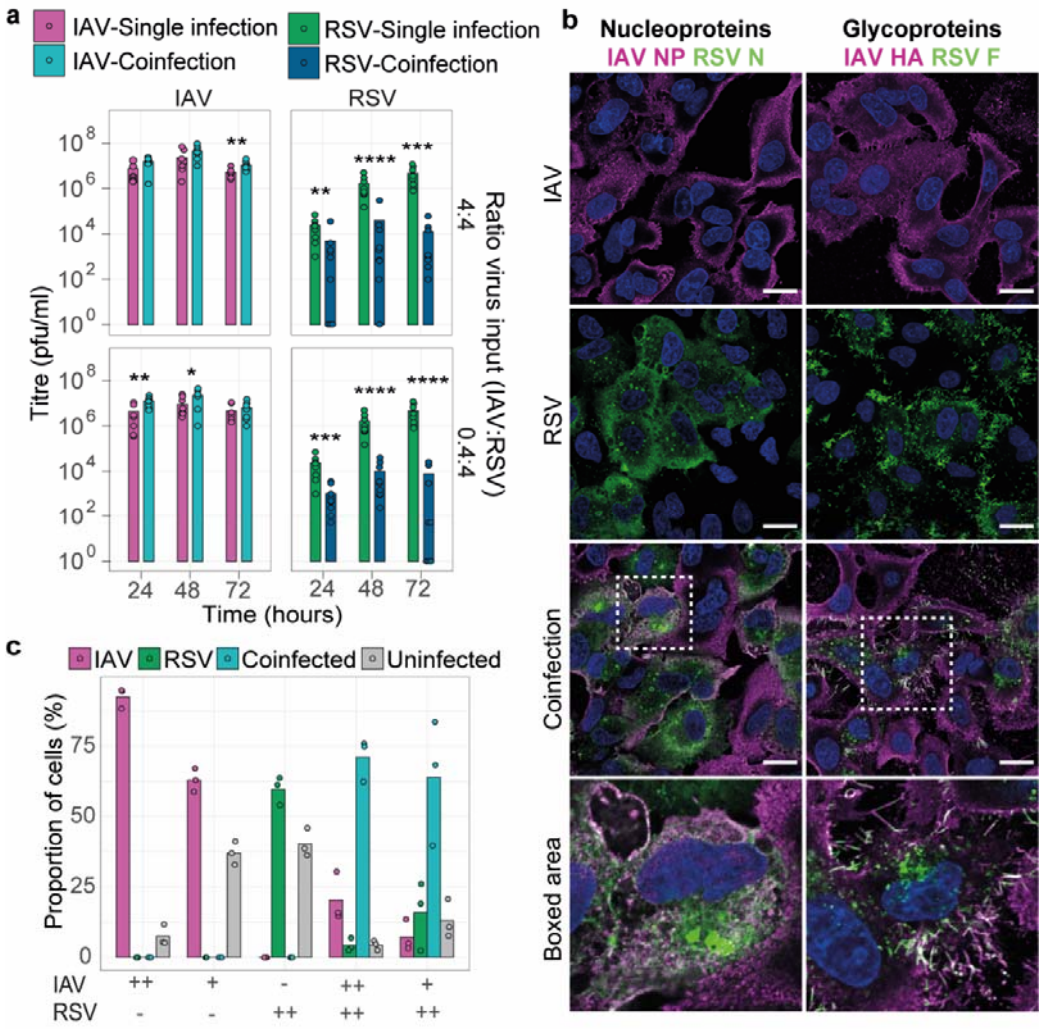

Figure 1. Replication kinetics and levels of cellular infection are affected in IAV and RSV coinfections. (a) Left panel, IAV replication kinetics in single infection (magenta bars) and mixed infection with RSV (teal bars). Right panel, RSV replication kinetics in single infection (green bars) and mixed infection with IAV (blue bars). Top row, infections carried out at equivalent MOI (4:4), bottom row, IAV input 10-fold less than RSV input (0.4:4). Error bars represent standard error, significance determined by Mann-Whitney test, * $p<0.05$, ** $p<0.01$, *** $p<0.001$, **** $p<0.0001$, non-significance not indicated. (b) Single or coinfected A549 cells were fixed at 24 hpi and stained by immunofluorescence for IAV nucleoprotein (magenta) and RSV nucleoprotein (green) (left column) and IAV haemagglutinin (magenta) and RSV fusion glycoprotein (green) (right column). Nuclei are stained with DAPI (blue). White boxes indicate regions in labelled boxed area, scale bar indicates 20 µm. (c) Percentage of cells infected with IAV-only (magenta), RSV-only (green), coinfected (teal) or uninfected (grey) in

single virus infection or mixed at 24 hpi. Panel below plot represents the infection conditions used: - for no virus, ++ for MOI 4 and + for MOI 0.4.

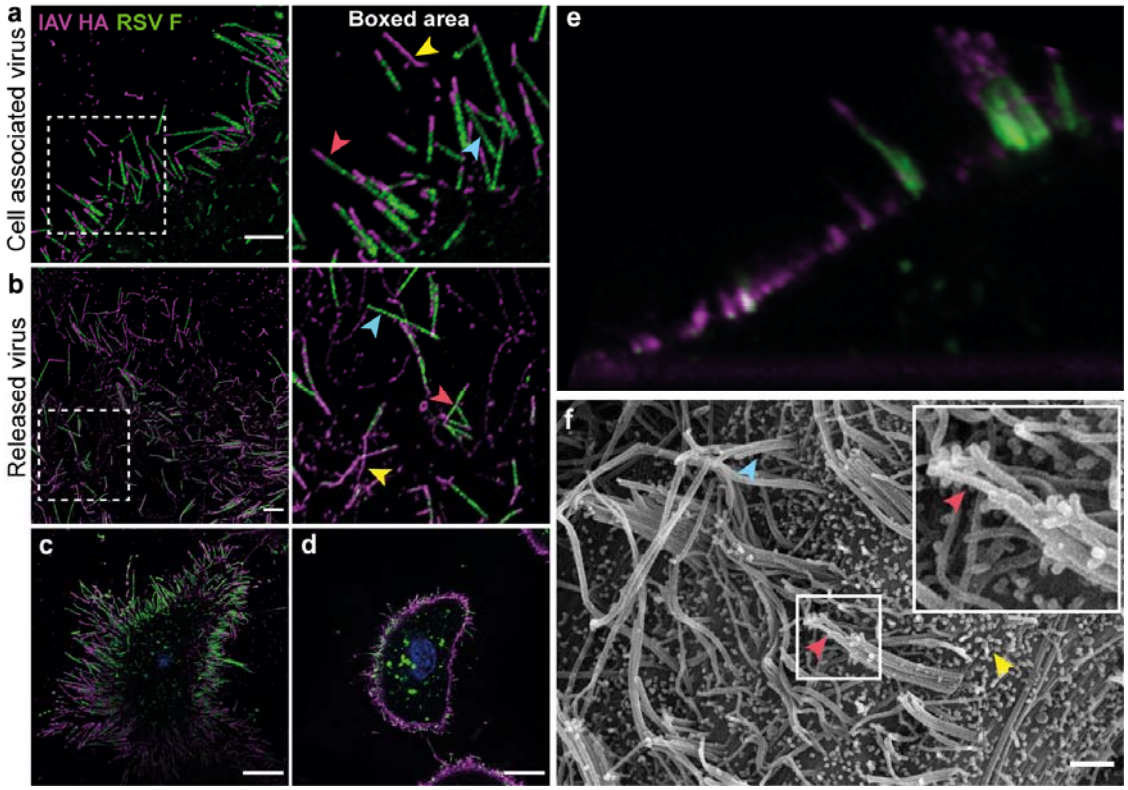

Figure 2. Coinfected cells display budding viral particles incorporate elements of both IAV and RSV. Cell associated viral filaments positive for IAV HA (magenta on merged image) and RSV F (green on merged image) that are cell associated (a) or released (b) from coinfected cells, imaged by super-resolution microscopy. Magnified images of white boxed regions indicate examples of IAV filaments (yellow arrows), RSV filaments (blue arrows) and dual-positive filaments (red arrows). Scale bars indicate 500 nm. (c and d) Coinfected cell exhibiting extensive dual-positive filament formation. Cell imaged by confocal microscopy at two Z-positions: basal side adhered to coverslip (c) and through the centre of the cell (d). Scale bars indicate 10 µm. (e) 2D z-plane image reconstructed from a Z-stack of a live cell stained for IAV HA and RSV F, imaged by super-resolution confocal microscopy at 100 nm intervals through the entire cell (16.3 µm). (f) Scanning electron micrograph of coinfected cell surface. IAV and RSV particles are indicated by yellow and blue arrows respectively. Red arrow and magnified region highlight particles that contain structural features of both IAV and RSV. Scale bar indicates 1 µm.

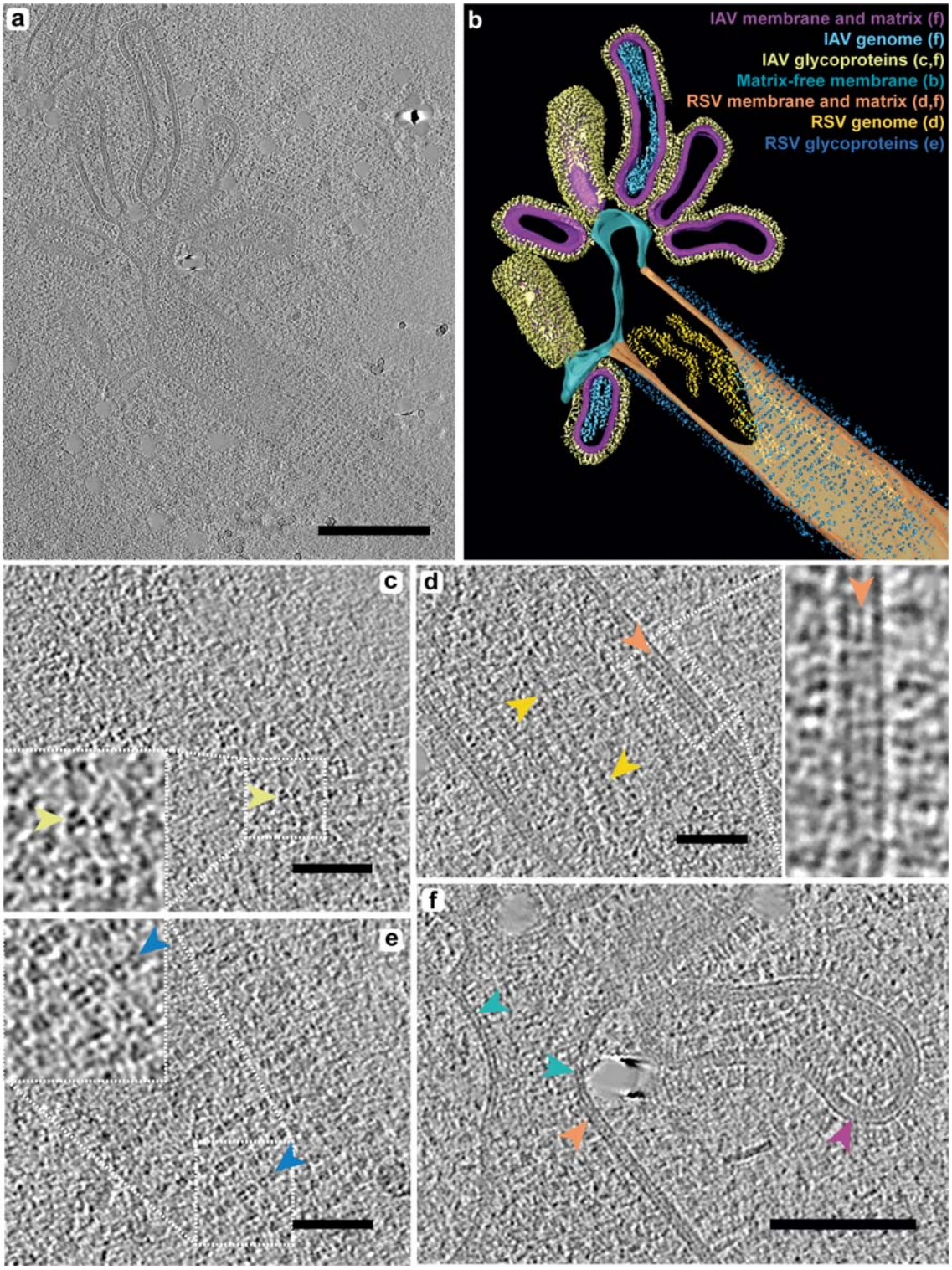

Figure 3: Coinfected cells produce hybrid viral particles that contain IAV- and RSV- like structural regions. Viral particles produced from coinfected A549 cells were frozen at 24 hpi and imaged by cryo-ET. (a) Cryo-tomogram showing an example of a hybrid viral particle. Particles consisted of an RSV-like region, extending to multiple IAV-like protrusion from the distal end of the filament. Scale bar indicates 200 nm. (b) Manual segmentation of the cryo-

703 tomogram shown in (a) highlighting examples key structural features (not all features have
704 been segmented). Coloured labels on figure match-coloured segmented volumes and letters
705 denote figure panels in which detailed images of features are shown. (c) The surface of IAV
706 region shows the ordering of IAV glycoproteins (yellow arrow). Magnified insert shows
707 density associated with HA trimers in a characteristic triangular arrangement. (d) Cross-section
708 through the RSV region shows RNPs, indicated by gold arrows. The inset image shows
709 magnified region highlighted by white dashed box, showing the RSV viral envelope associated
710 with the matrix layer (orange arrow). (e) The surface of RSV region shows the characteristic
711 helical arrangement of glycoproteins into rows (blue arrows). The magnified insert shows
712 circular density corresponding to RSV glycoproteins. Scale bars in panels (c-e) indicate 50 nm.
713 (F) IAV- and RSV-like regions were joined by a continuous membrane bilayer. Coloured
714 arrows indicate presence or absence of matrix layer. Membrane in IAV and RSV region was
715 clearly associated a with matrix layer, indicated by orange and magenta arrows for RSV and
716 IAV respectively, whilst matrix appeared absent in the adjoining regions (blue arrow). Scale
717 bar indicates 100 nm.

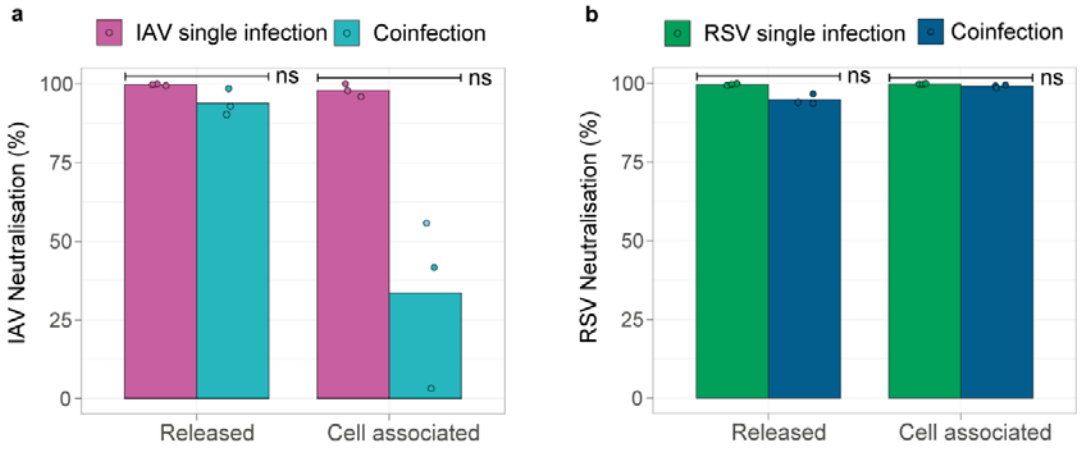

718

719 **Figure 4: Virus produced from coinfection facilitates evasion of neutralising antibodies**
720 **by IAV, but not by RSV.** Virus harvested from coinfection or single infections was pre-
721 incubated with serum targeting IAV HA, RSV F or a serum-free control, and then used to infect
722 A549 cells. Infections were fixed and immunostained at 12 hpi and the number of IAV infected
723 cells was quantified using an automated image-based cell counter. (a) Neutralisation of IAV
724 by polyclonal antisera targeting IAV HA when virus was harvested from the supernatant or
725 cell pellet fractions of a single IAV infection (magenta bars) or a coinfection (teal bars).
726 Neutralisation was calculated as a percentage of IAV infected cells in the wells containing
727 serum compared to matched serum-free controls. Statistical significance calculated by Mann

728 Whitney test, ns indicates p>0.05. (b) Neutralisation of RSV by Palivizumab (targeting RSV
729 F) when virus was harvested from the supernatant or cell pellet fractions of a single RSV
730 infection (green bars) or a coinfection (dark blue bars). Neutralisation calculated as a
731 percentage of RSV infected cells in the wells containing serum compared to matched serum-
732 free controls. Data was collected from three independent experiments and statistical
733 significance calculated by Mann Whitney test, ns indicates p>0.05.

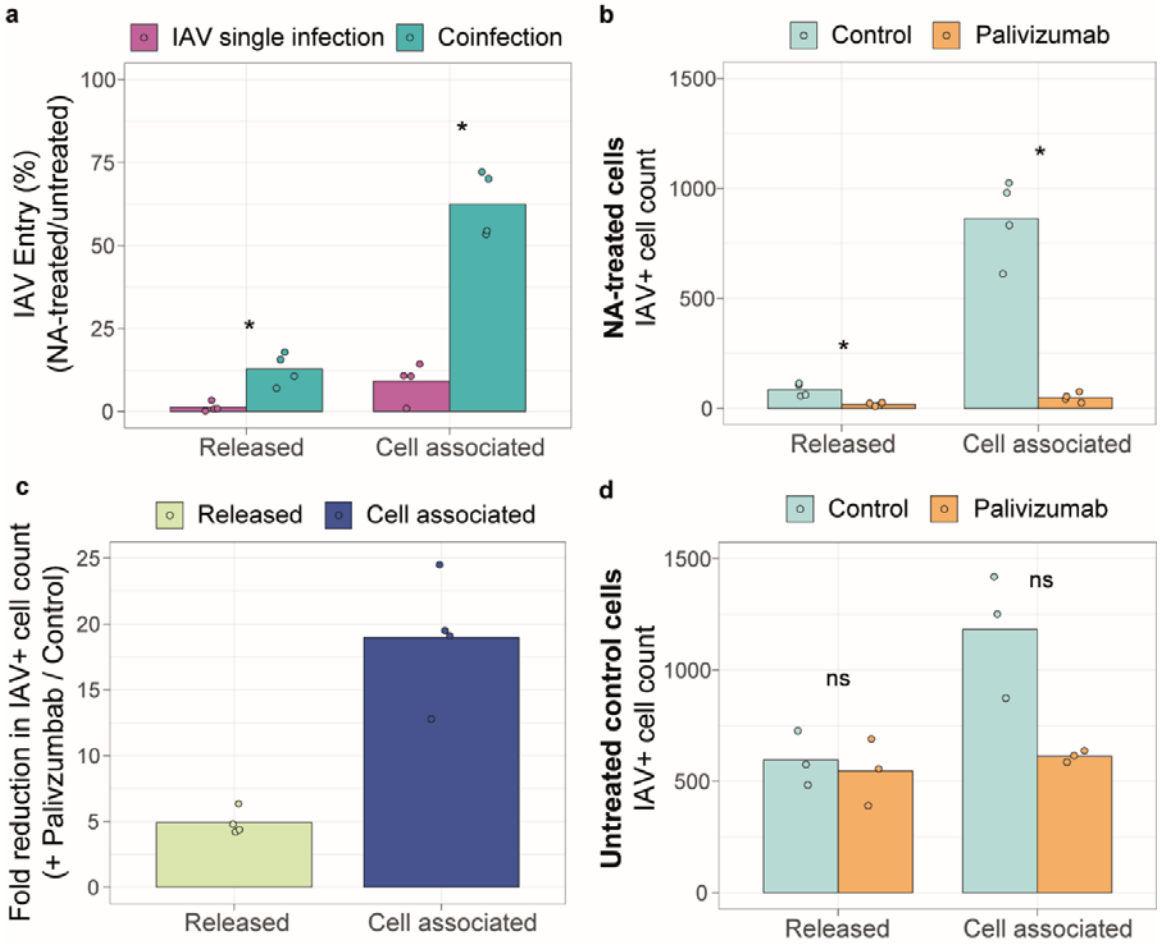

734

735 **Figure 5. Virus produced from coinfection facilitates IAV infection in sialic acid-depleted**
736 **cells.** NA-treated or control A549 cells were infected with virus harvested from coinfection or
737 IAV single infection, fixed and immunostained at 12 hpi and the number of IAV infected cells
738 was quantified using an automated image-based cell counter. (a) Ratio of IAV entry into NA-
739 treated cells versus control cells when harvested from single infection (magenta bars) or mixed
740 infection (teal bars). IAV entry to NA-treated cells was calculated as a percentage of the IAV-
741 positive cell count in the matched untreated control. (b) IAV positive cell count in NA-treated
742 cells infected with virus that was harvested from coinfection and incubated with palivizumab
743 (orange bars) or a serum free control (cyan bars). (c) Fold change in IAV positive cell counts
744 as shown in (e) for released (yellow bar) and cell associated (navy bar) virus. (d) IAV positive

745 cell count in untreated control cells infected with virus that was harvested from coinfection and
746 incubated with palivizumab (orange bars) or a serum free control (cyan bars). Data was
747 collected from three independent experiments and statistical significance was determined by
748 Mann Whitney test, * indicates $p<0.05$ and ns indicates $p>0.05$.

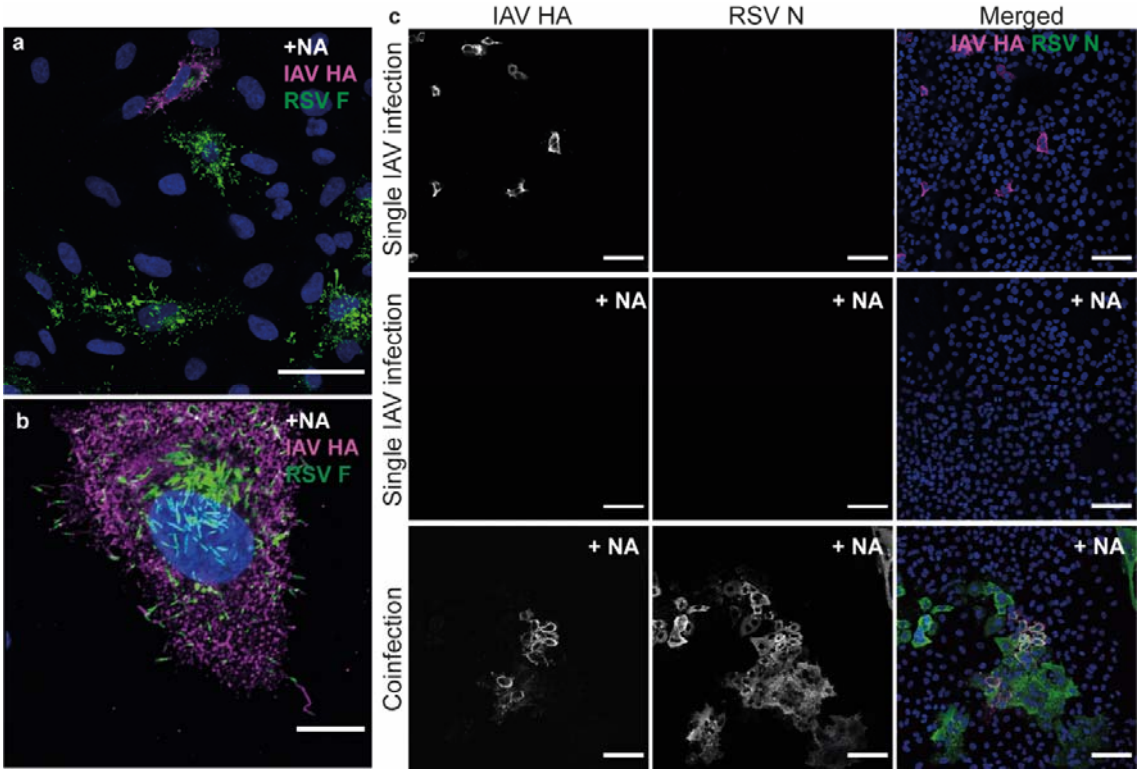

749

750 **Figure 6: Hybrid viral particles possess dual infectivity for IAV and RSV and can**
751 **facilitate spread of IAV in a refractory cell population.** (a) A549 cells were infected with
752 cell-associated virus from a coinfection and incubated for 12 hpi, before staining for IAV HA
753 (magenta) and RSV F (green) and imaging by standard confocal microscopy. Scale bar
754 indicates 100 µm. (b) Super-resolution confocal imaging of coinfected cells shows formation
755 of dual-positive filamentous structures, indicating hybrid particle formation is maintained upon
756 passage. Scale bar indicates 1 µm. (c) Virus harvested from IAV single infection (top and
757 middle rows) or coinfection (bottom row) was incubated on untreated control wells (top row)
758 or neuraminidase-treated wells (middle and bottom rows) with an overlay for 48 hours. Foci of
759 infection were immunostained for IAV HA (magenta) and RSV N (green) and imaged by
760 confocal microscopy. Infection was observed by IAV from single infection in untreated control
761 cells, but not neuraminidase-treated cells. Virus harvested from coinfection formed large foci
762 and IAV foci colocalised with RSV foci. Scale bar indicates 200 µm.

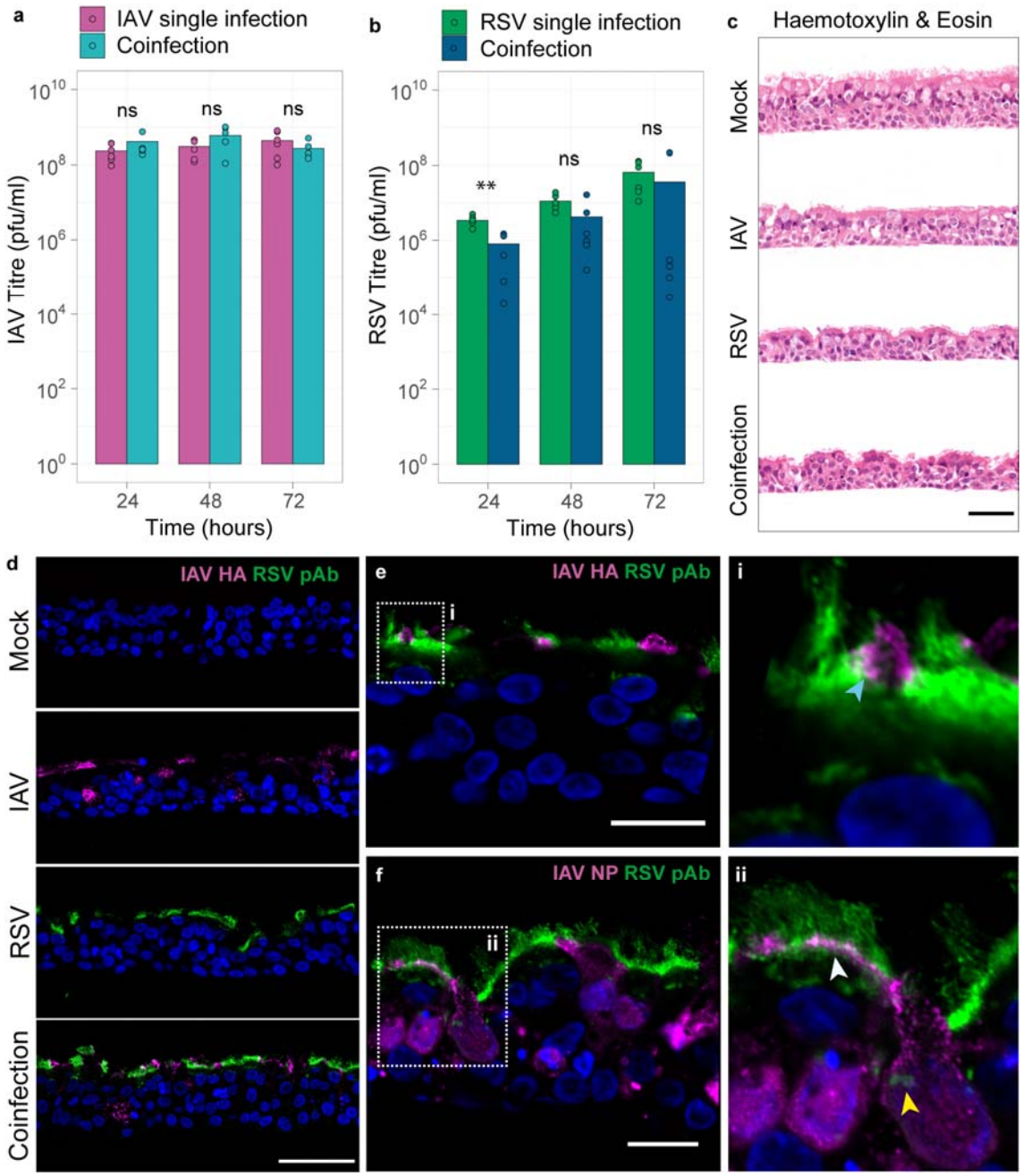

Figure 7: Coinfection of primary differentiated human bronchial epithelial cell cultures (hBECs) results in robust replication of IAV and RSV, with evidence of cellular coinfection. (a) IAV replication kinetics in hBEC cultures in single infection (magenta bars) and mixed infection with RSV (teal bars), n=6 individual transwells over 3 independent experiments. (b) RSV replication kinetics in hBEC cultures in single infection (green bars) and mixed infection with RSV (dark blue bars). n=6 individual transwells over three independent experiments. (c) Paraffin embedded sections collected at 24 hpi, stained with haemotoxylin and eosin. (d) Immunofluorescence showing IAV HA (magenta) and RSV antigen (green) localisation in paraffin embedded sections at 24 hpi. (e) Coinfected section imaged by super-

773 resolution confocal microscopy shows localisation of IAV HA (magenta) and RSV antigen
774 (green) to the apical surface of epithelial cells. Scale bar represents 20 µm. The magnified area
775 (i) shows the region indicated by the white dashed box, highlighting a coinfected cell with IAV
776 HA and RSV antigen localised at apical surface (blue arrow). (f) Localisation of IAV NP
777 (magenta) and RSV antigen (green) within coinfected cells. Scale bar represents 20 µm. The
778 magnified area (ii) shows the region indicated by the white dashed box highlighting IAV NP
779 and RSV antigen within the cytoplasm, where RSV inclusion bodies can be observed (yellow
780 arrow), and at the apical surface of coinfected cells (white arrow).

781 **Movie 1**: Video showing serial sections through the z-axis of a tomogram of a hybrid particle
782 with a multiple IAV region, formed during coinfection of IAV and RSV (corresponding image
783 shown in Fig. 3). Glycoproteins and RNPs of both IAV and RSV are labeled and denoted by
784 arrows.

785 **Movie 2**: Video showing serial sections through the z-axis of a tomogram of hybrid particle
786 with IAV and RSV regions with an adjoining region with a clear lumen (corresponding image
787 shown in Extended data Fig. 4C). Glycoproteins and RNPs of both IAV and RSV are labeled
788 and denoted by arrows.

789 **Movie 3**: Video showing serial sections through a tomogram of a pseudotyped viral filament
790 generated during IAV and RSV coinfection (corresponding image shown in Extended data Fig.
791 3). Glycoproteins and RNPs are labeled and denoted by arrows.

792

793

794 **Extended Data**

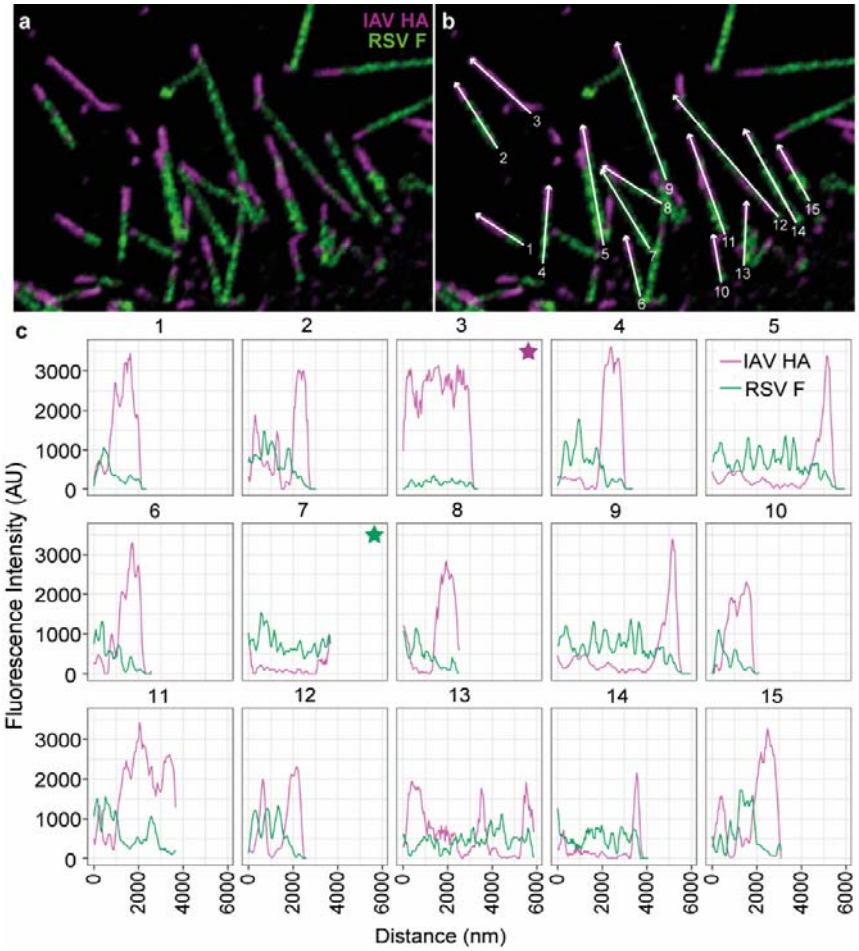

795

796 **Extended Data Figure 1: HA and F are expressed in discrete patches along the length of**
797 **filaments, with HA predominantly at the distal end.** (a) Magnified view of cell associated
798 filaments (full image shown in figure 2A) show filaments with distinct patches of IAV HA
799 (magenta) and RSV F (green) glycoproteins along the length of the filaments. (b) White arrows
800 and filament numbering correspond to fluorescence intensity profiles displayed in (c). Minimal
801 colocalisation was observed in the fluorescence intensity profiles (c) for IAV HA (magenta
802 line) and RSV F (green line) signal along filaments numbered 1-15. IAV (filament 3, magenta
803 star) and RSV (filament 7, green star) filaments were also identified among dual positive
804 filaments.

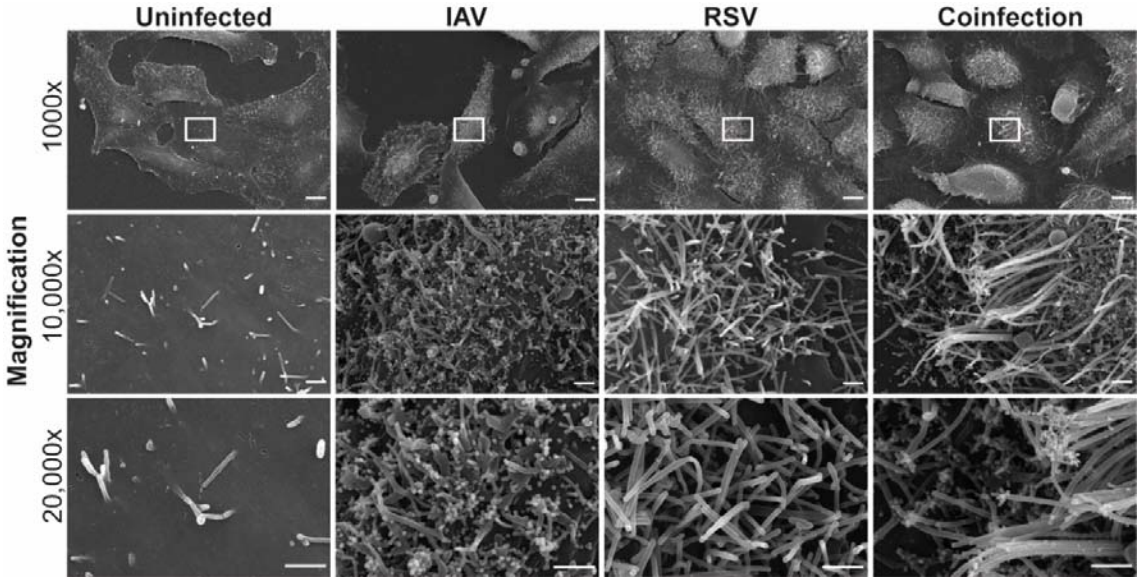

Extended Data Figure 2: Scanning electron microscopy shows clear differences between IAV and RSV virion structure. Scanning electron micrographs of IAV, RSV, coinfected or mock infected cells imaged at 1000x (top row), 10,000x (middle row) and 20,000x (bottom row), region of magnification is denoted by the white box. Scale bars represent 10 µm at 1000x and 1 µm at 10,000x and 20,000x magnification.

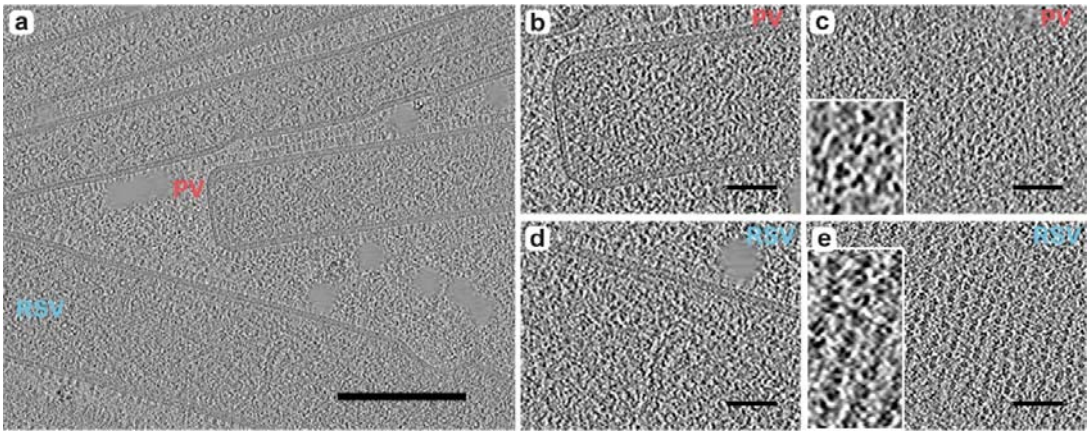

Extended Data Figure 3: Coinfection generates RSV filaments that are pseudotyped with IAV envelope proteins. (a) Tomogram shows a pseudotyped RSV filament, indicated by red 'PV' label, near to RSV filaments, one example indicated by blue 'RSV' label. Scale bar indicates 200 nm. (b) Magnified cross-section of end of pseudotyped filament, showing RSV RNP contained within virion. (c) Surface of psuedotyped filament shows irregular arrangement of glycoproteins, with many displaying characteristic triangular shape of HA trimers, shown in magnified inset image. (d) Magnified cross-section of end of RSV filament, showing RSV RNP

contained within virion and ultra-structure consistent with the pseudotyped virion. (e) Surface of the RSV filament shows helical arrangement of glycoproteins, with ring-shaped density of glycoproteins highlighted in magnified insert. Scale bars in panels (b-e) indicate 50 nm.

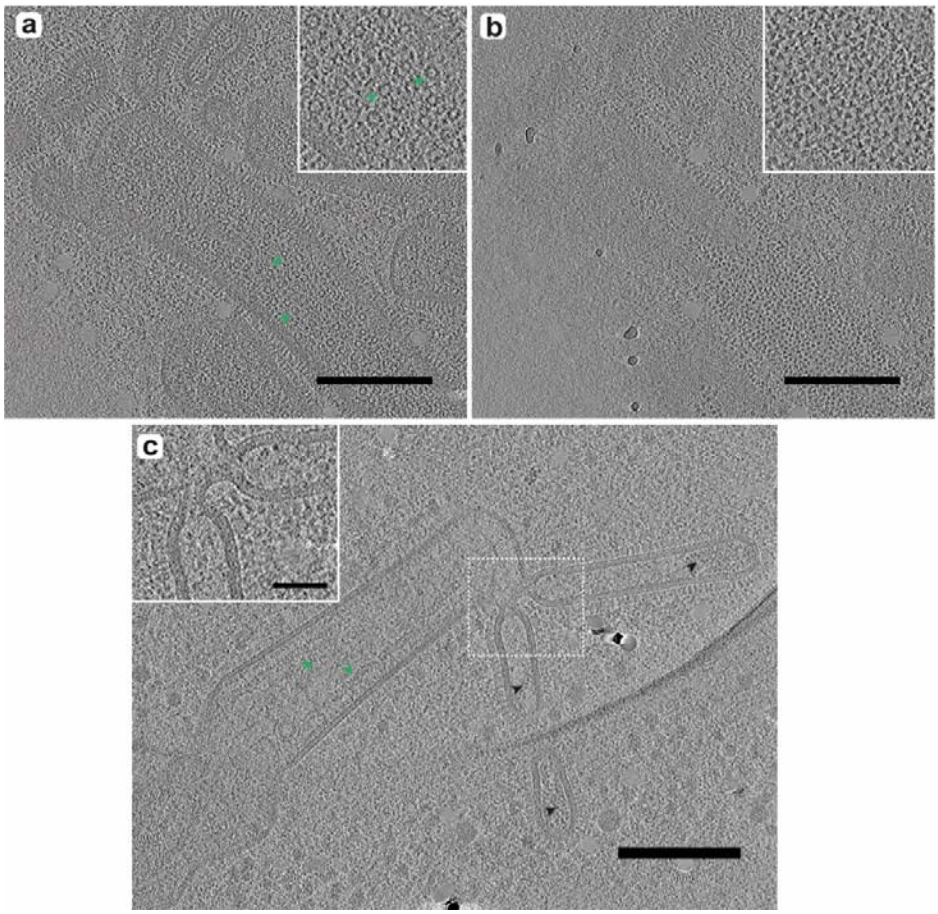

Extended Data Figure 4: Further examples of hybrid particles. (a and b) show two z-positions through the same hybrid particle, which also displays pseudotyping in RSV-like region. (a) IAV-like regions extend from the top of the filament and ring-shaped densities corresponding to RSV genome, indicated by green arrows and highlighted in magnified inset image, are present within the virion. (b) The surface of the virion is covered in glycoproteins that are consistent in shape and arrangement with IAV glycoproteins, highlighted in magnified inset. Scale bars indicate 200 nm. (c) Tomogram shows a further example of a hybrid particle with two IAV-like regions which are joined to the RSV-like region by a continuous membrane. Black and green arrows indicate IAV and RSV RNP respectively, contained with in their associated structural regions. Scale bar indicates 200 nm. There is a clear shared lumen which continues between RSV and IAV regions, highlighted within magnified inset which corresponds to region marked by white dashed box. Scale bar indicates 50 nm.

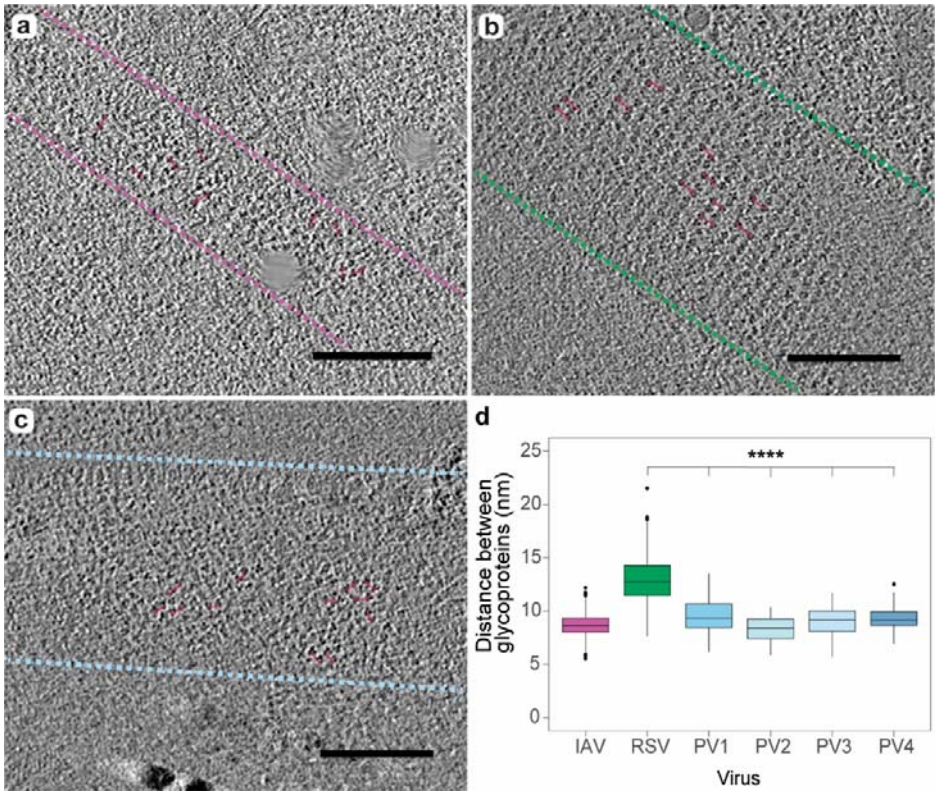

Extended Data Figure 5. Inter-spike distance measurements reveal that pseudotyped viruses are decorated with IAV glycoproteins. To determine the glycoprotein arrangement on pseudotyped viruses, inter-spike distances were measured between glycoprotein pairs. Representative examples are shown for IAV (a), RSV (b) and pseudotyped virions (c) with red lines indicating example distances measured. Pink, green and blue dashed lines indicate the edges of IAV, RSV and psuedotyped filaments respectively. Scale bars indicate 200 nm. Control measurements were collected from 11 tomograms for IAV (measurements n=326) and 11 tomograms for RSV (measurements n=236). Measurements of pseudotyped virions were collected from 4 individual tomograms (n=50 measurements per tomogram). (d) Unpaired t-test analysis confirmed glycoproteins distance measurements were significant different between RSV and pseudotyped virions, with average inter-spike distances of 8.71 nm for IAV, 12.9 nm for RSV and a range of 8.31-9.56 nm for pseudotypes.

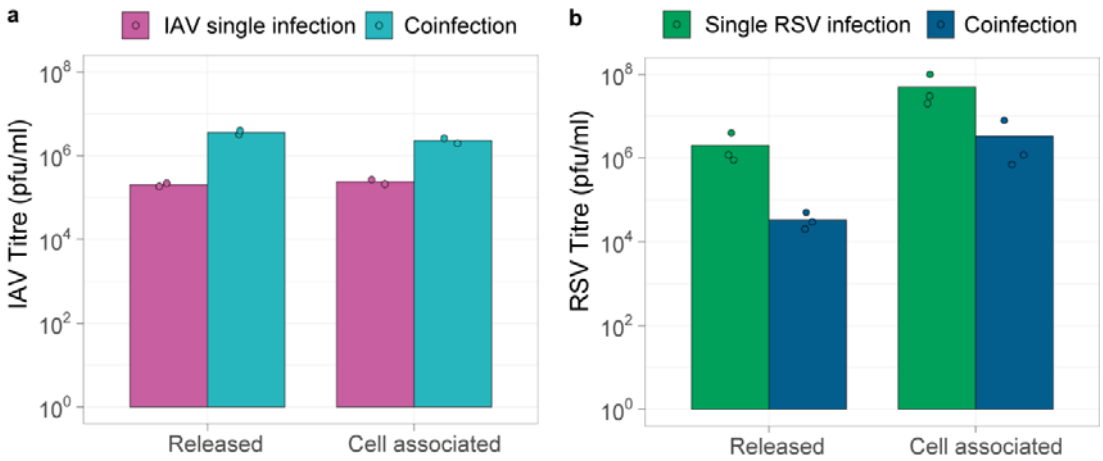

852

853 **Extended data figure 6: Supporting data for neutralisation assays.** Quantification of viral
854 input to neutralisation assays. Virus was harvested from supernatant (released) and cell
855 associated fractions of single or coinfected A549 cells and transferred to neutralisation assays.
856 The same virus stocks were then back titrated to determine infectious viral input. (a) Back
857 titration of IAV in single infection (magenta bars) or coinfection (teal bars) by IAV plaque
858 assay. (b) Back titration of RSV in single infection (green bars) or coinfection (dark blue bars)
859 by RSV plaque assay.

860

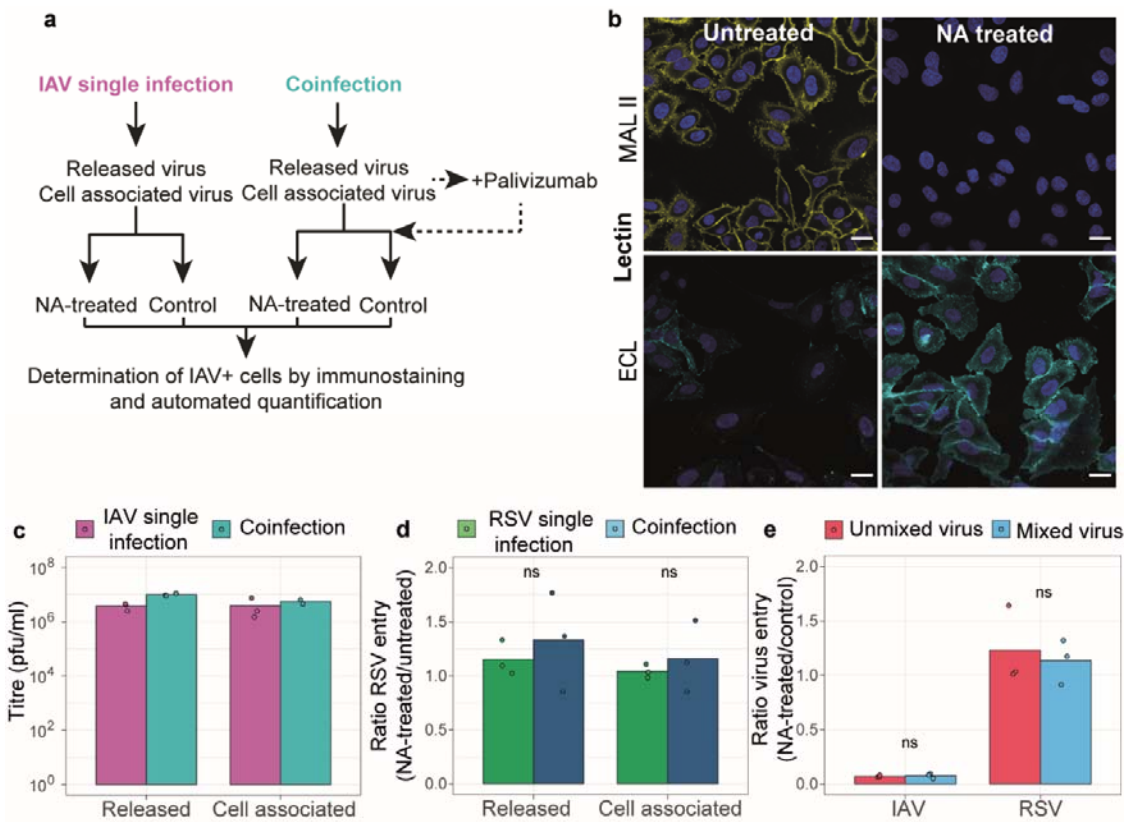

861

Extended Data Figure 7: Supporting data for neuraminidase experiment. (a) Schematic demonstrating experimental design. (b) NA-treated and untreated cells stained with Maackia Amurensis Lectin II (MAL II) in yellow (top row) and Erythrina Cristagalli Lectin (ECL) in cyan (bottom row). (c) Viral input in pfu/ml of IAV as determined by back-titration of inoculum for NA-experiment by IAV plaque assay. (d) Ratio of RSV entry into NA-treated cells versus control cells when harvested from single infection (green bars) or mixed infection (blue bars). RSV entry to NA-treated cells was calculated as a percentage of the RSV-positive cell count in the matched untreated control. (e) Ratio of virus entry of IAV only or RSV only (red bars) into NA-treated over control cells, compared to entry of IAV pre-mixed with RSV or RSV pre-mixed with IAV into NA-treated over control cells (blue bars). Statistical significance was determined by Mann Whitney test, ns indicates $p>0.05$.

Extended Data File

Description of IAV and RSV particles

We identified structures consistent with IAV filaments and pleiomorphic particles that were densely coated with glycoproteins (Fig. 1A, Video S1). IAV filaments varied in length, with an average diameter of 84.8 (+/-6.97) nm. IAV ribonucleoproteins (RNPs) could be observed within pleomorphic virions (Figure 1A, Supplementary Video S1). We also identified RSV filaments (Figure 1B, Supplementary video S2) with an average width of 158 (+/-14.6) nm, but many irregular shaped virions were also observed (Fig. 2). Differences in glycoprotein distribution as well as RNP structure between RSV and IAV virions were evident. The glycoproteins in RSV virions exhibited sparser distribution along the virion than IAV glycoproteins (Figs. 1C and 1D). RNPs could be clearly seen in many IAV and RSV filaments. While IAV comprised a single ordered set of RNPs in a "7+1" arrangement at the distal end of filaments, multiple RNPs were detected within RSV filaments having herringbone morphology and ring-like structures attributed to be nucleocapsid (N) or N-RNA assemblies (*23, 52, 53*) (Fig. 1A-D, Fig. 2). Upon closer inspection of glycoproteins on the surface of virions (top and bottom slices in the tomograms), distinct patterns of glycoprotein arrangement were observed between the two viruses. In IAV virions, glycoproteins were densely packed, devoid of any long-range order, with the "triangular-shaped" trimeric head of HA clearly visible (Fig. 1E, 1F, Fig. 3). However, RSV exhibited a more symmetrical helical arrangement of glycoproteins (striped layers of density) with specific clustering in pairs (Fig. 1G, 1H, Fig. 3).

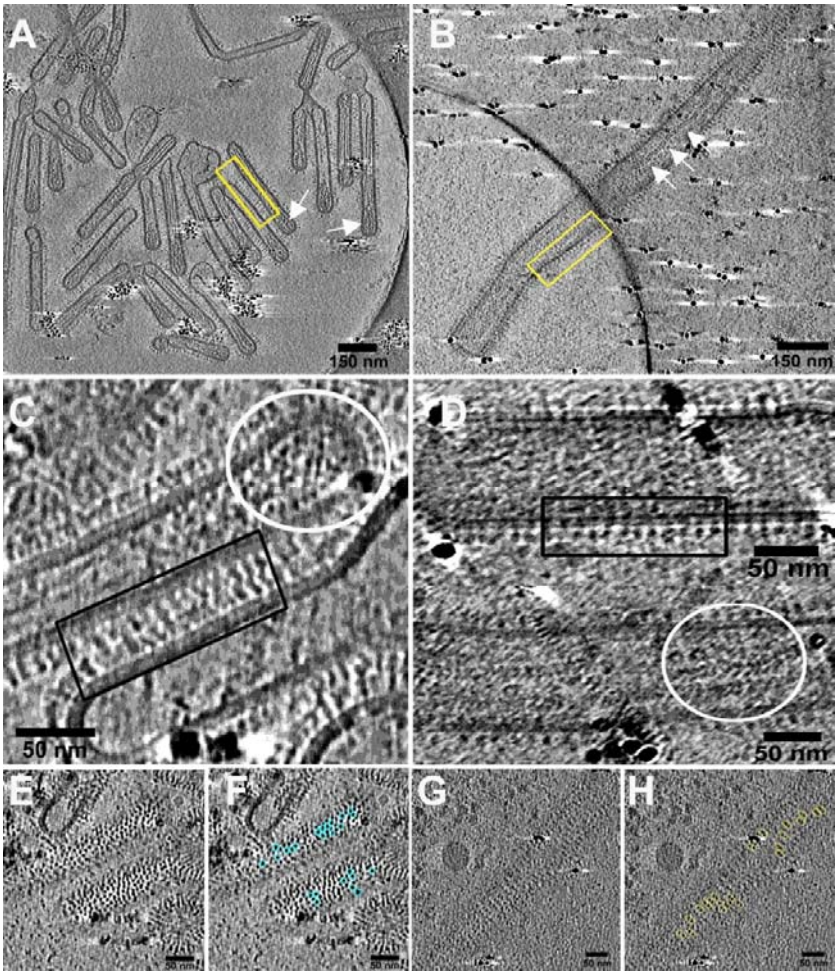

Fig. 1. Cryo-ET shows differences in glycoprotein ordering and RNP organisation between IAV and RSV virions. Cryo-electron tomograms of IAV (**A**) and RSV **(B)** denote pleomorphic morphology alongside differences in glycoprotein and RNP organisation (yellow rectangle and white arrows). IAV virions exhibit a single set of ordered RNPs (**C**, white circle) while multi genomes can be seen in RSV virions (**D**, white circle). Glycoproteins can be seen in a picket fence like distribution along the viral membrane, although more densely packed in IAV than RSV (**C** and **D**, black rectangles). Looking at the glycoproteins from the top and bottom of the virions, significant differences are visible in glycoprotein packing: the triangular hemagglutinin HA spikes on IAV are densely packed with no long-range order (**E** and **F**, cyan circles) while RSV shows clustering of glycoprotein pairs (**G** and **H**, yellow ellipses).

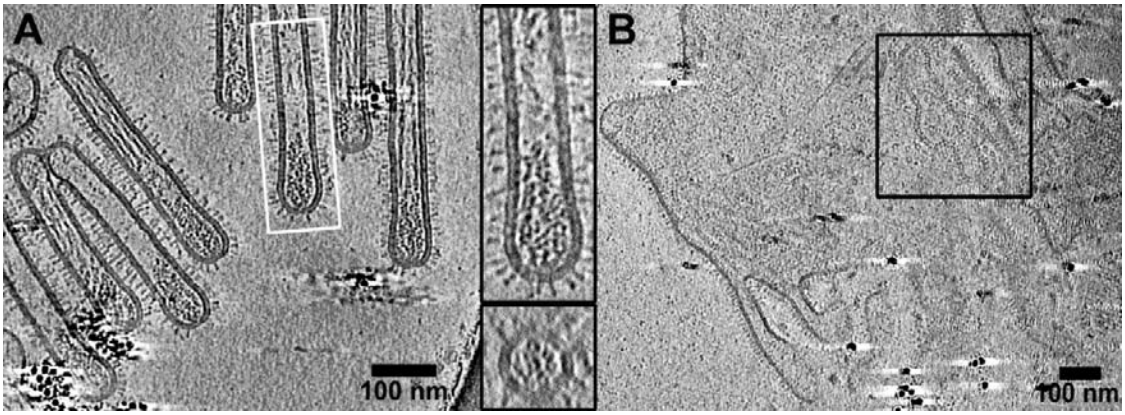

Figure 2. **Distinct RNP organization in IAV and RSV virions seen by Cryo-ET.** (**A**) IAV shows a single ordered set of RNPs at the distal end (white rectangle and magnified view of the same) of filaments. Transverse section (bottom image, magnified view of the white rectangle) of the filament denotes the "7+1" arrangement of RNPs in IAV virions. (**B**) Although RSV can form irregular shaped virions in addition to filaments, they are filled with multiple RNPs inside and decorated with spikes on the outside.

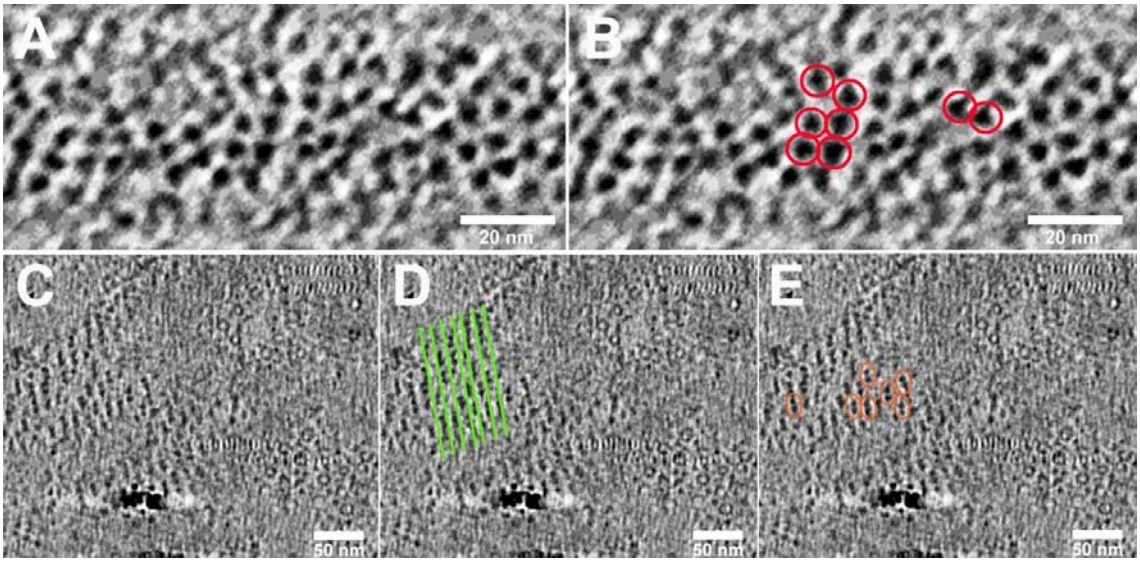

Figure 3. **Different glycoprotein ordering between IAV and RSV virions.** Inspection of top and bottom views of glycoprotein spikes (corresponding to top and bottom slices of the tomograms) on IAV and RSV virions indicates a different pattern of organization. (**A** and **B**) While the triangular heads (red circles) of the HA glycoprotein in IAV is clearly visible, the spikes are densely packed and devoid of any long-range order. (**C-E**) On the other hand the spikes on RSV appear to be helically ordered as seen by the striped arrays of density (**D**) and specific (**E**) clustering of glycoproteins in pairs (red ellipses) is clearly evident.

Extended Data Movie 1. Video showing serial sections through the z-axis of a tomogram of IAV virions exhibiting pleomorphic morphology. Glycoproteins and RNPs are labelled and denoted by arrows.

Extended Data Movie 2. Video showing serial sections through the z-axis of a tomogram of an RSV filament. Glycoproteins and RNPs are labelled and denoted by arrows.